TEAD promotes lineage progression of subpallial neural progenitor cells independent of YAP/TAZ

Charles H. Perry[1,4], Alfonso Lavado[1,3,4], Venkata Thulabandu[1], Cody Ramirez[1], Joshua Paré[1], Rajiv Dixit[1], Akhilesh Mishra[2,5], Jiyuan Yang[2], Jiyang Yu[2] & Xinwei Cao[1,*]

[1]Department of Developmental Neurobiology, [2]Department of Computational Biology, [3]Center for Pediatric Neurological Disease Research, Pediatric Translational Neuroscience Initiative, St. Jude Children's Research Hospital, Memphis, TN 38105, USA. [4]These authors contributed equally: Charles H. Perry, Alfonso Lavado. [5]Current address: Department of Life Science, National Institute of Technology, Rourkela 769008, Odisha, India.
*e-mail: Xinwei.cao@stjude.org

Abstract

The embryonic ventral telencephalon (subpallium) gives rise to extremely diverse types of cells. Although it is known that subpallial neural progenitors possess characteristics distinct from their cortical counterparts, the mechanisms governing their lineage progression are poorly understood. Here we show that TEAD, the key DNA-binding factor of the Hippo pathway, promotes lineage progression of subpallial neural progenitors; the loss of TEAD1 and TEAD2 (TEAD1/2) during mammalian brain development expands early progenitors and reduces late progenitors uniquely in the subpallium, but not in the cortex. Importantly, this function of TEAD1/2 is independent of their canonical partners in the Hippo pathway, transcriptional coactivators YAP and TAZ (YAP/TAZ), as YAP/TAZ loss leads to the opposite phenotype—a depletion of early progenitors and increase in late progenitors. We further show that TEAD1/2 act by, at least in part, inhibiting Notch signaling and by cooperating with INSM1. It has been shown that orthologs of TEAD and INSM1 cooperate to regulate neuronal cell fate decisions in worms and flies. Our study reveals a remarkable evolutionary conservation of the function of this transcription factor complex during metazoan neural development.

Keywords: radial glia, intermediate progenitor, apical progenitor, basal progenitor, subapical progenitor, neurogenesis, interneuron, basal ganglia, medial ganglionic eminence (MGE), VGLL4

Introduction

The telencephalon in all vertebrates consists of two main territories: the pallium (dorsal telencephalon, cortex) and the subpallium (ventral telencephalon)[1]. The embryonic subpallium is subdivided into four major anatomical regions: the lateral, medial, and caudal ganglionic eminences (LGE, MGE, and CGE, respectively) and the anterior entopeduncular area (AEP)[2].The cell types produced by the subpallium during development are extremely diverse, which include not only neurons and glia that form the basal ganglia, parts of the septum and the amygdala, the preoptic area, but also all cortical interneurons and a subset of cortical oligodendrocyte lineage cells (OLCs)[1-4].

In the developing central nervous system (CNS), the primary stem/progenitor cells, neuroepithelial cells (NECs) and the cells they transform into upon the onset of neurogenesis—radial glia (RG), form the ventricular zone (VZ) lining the central lumen of the neural tube[5,6]. These cells divide—depending on their division mode—to expand or replenish themselves, produce neurons directly (direct neurogenesis), or give rise to another type of progenitor cells known as intermediate progenitors (IPs). IPs, residing in the subventricular zone (SVZ) adjacent to the VZ, divide to expand themselves and produce neurons (indirect neurogenesis), increasing the cell output of primary stem/progenitor cells. NECs/RG and IPs exhibit key cell biological differences. NECs/RG undergo mitosis at or near the ventricular surface (VS); they are also called apical progenitors (APs). IPs undergo mitosis in the SVZ; they are also called basal progenitors (BPs). Moreover, it is generally thought that RG are multipotent (being able to produce different types of neurons or both neurons and glia), whereas IPs are unipotent (being able to produce only one type of neurons), and that RGs divide more rounds than IPs.

Our knowledge about RG and IPs is mostly obtained by studying progenitor cells in the developing mouse cortex. Subpallial neural progenitors, however, are likely to possess unique features that underlie their distinct cellular output in terms of cell number and cell type diversity. For example, whereas the vast majority of progenitor cells reside in the VZ in most regions of the developing mouse CNS, in the ganglionic eminences (GEs) the SVZ largely surpasses the VZ in size and is the main site of cell proliferation throughout most of the neurogenic period[7-9]. Furthermore, studies have found novel subtypes of progenitor cells (e.g., subapical progenitors (SAPs), which are common in the mouse GEs and in the developing gyrated cerebral cortices of ferrets and sheep but rare in the developing mouse cortex) and distinct progenitor behaviors (e.g., more proliferative divisions by several subtypes of progenitor cells and a progressively faster cell cycle) in the subpallium[9]. It remains largely unknown what mechanisms uniquely govern the characteristics and lineage progression of subpallial neural progenitor cells.

68 The Hippo pathway plays important roles in the development, tumorigenesis, and
69 regeneration of many tissues across species[10]. It controls the activity of a transcription factor
70 complex composed of the transcriptional coactivator YAP (Yorki in flies, YAP and TAZ
71 (YAP/TAZ) in mammals) and the DNA-binding factor TEAD (Scalloped in flies, TEAD1–4 in
72 mammals). In many tissues, YAP is expressed in the stem/progenitor cells and promotes their
73 proliferation and self-renewal[11,12]. We have shown that, during mammalian cortical
74 development, YAP/TAZ maintain the proliferative potential of RG[13]. In contrast to the extensive
75 studies on the functions of YAP/TAZ, studies on the in vivo function of TEAD in mammals are
76 scarce[14,15], probably because it is assumed that TEAD simply acts as the DNA-binding partner
77 of YAP/TAZ. Some observations, however, suggest that TEAD acts with other cofactors in some
78 contexts. TEAD is evolutionarily much more ancient than YAP; TEAD is present in
79 amoebozoans whereas YAP appears to be restricted to holozoans[16,17]. In *Drosophila*,
80 Scalloped, identified in 1929 as a result of a wing phenotype[18], regulates wing identity
81 independent of Yorki/YAP[19,20]. In *C. elegans*, the TEAD ortholog EGL-44 regulates neuron cell
82 fate and neuroblast lineage progression in an apparently YAP-independent manner[21-23]. We
83 have reported that, in the developing chick spinal cord, YAP is only expressed in the VZ but
84 TEAD is expressed not only in the VZ but also in nearby cells expressing the proneural
85 transcription factor Neurogenin 2 (Ngn2)[24], suggesting that TEAD may have YAP-independent
86 function in these Ngn2-expressing cells.
87 In this study, we show that TEAD promotes lineage progression of subpallial neural
88 progenitor cells. Notably, TEAD acts via a YAP/TAZ-independent mechanism. We further show
89 that TEAD acts at least in part by inhibiting Notch signaling and suggest that TEAD cooperates
90 with INSM1 (Insulinoma-associated 1), a zinc-finger transcription factor, in this developmental
91 context.
92

93 # Results

94 ## TEAD1 is expressed in broader regions than YAP/TAZ are in the developing
95 telencephalon

96 Our earlier observation in the chick neural tube prompted us to examine YAP/TAZ and TEAD
97 expression patterns in the developing mammalian telencephalon. We compared YAP/TAZ and
98 TEAD1 immunostaining patterns to those of SOX2, which marks RG and some IPs throughout
99 the developing CNS; TBR2, which marks cortical IPs[25]; and ASCL1, which marks subsets of
100 subpallial neural progenitors[26-28] (Fig. 1a). In the cortex, as we have reported previously[13],

101 YAP/TAZ were specifically expressed in SOX2^{+}TBR2^{-} RG. TEAD1 immunosignals, however,
102 were detected in the VZ, the TBR2-dense SVZ, and weakly above the SVZ, suggesting that
103 TEAD1 is expressed in both RG and IPs, and probably also in new-born neurons. In the MGE,
104 YAP/TAZ were expressed in the cells near the VS, presumably RG, whereas TEAD1 was
105 detected in both the VZ and the adjacent SVZ. YAP/TAZ and TEAD1 showed similar expression
106 patterns in the LGE and CGE (data not shown).
107 To further determine whether YAP/TAZ and TEAD1 are expressed in APs or BPs, we
108 co-immunostained YAP/TAZ or TEAD1 with the mitosis marker phospho-Histone H3 (pH3) (Fig.
109 1b), because mitosis position is a defining feature of APs and BPs. In the cortex, >90% of
110 YAP/TAZ^{+}pH3^{+} cells were found along the VS (apical) and a small fraction within the VZ away
111 from the VS (subapical) (Fig. 1c); the latter type of progenitors has been defined as SAPs—they
112 are derived from APs and give rise to BPs[9]. Among TEAD1^{+}pH3^{+} cells, only ~60% were found
113 along the VS, with the rest either within the VZ or in the SVZ (basal) (Fig. 1c). Similar patterns
114 were observed in the MGE, except that the fraction of those dividing apically was reduced by
115 ~10% for both YAP/TAZ^{+} cells and TEAD1^{+} cells (Fig. 1c). These results demonstrate that, in
116 the developing telencephalon, YAP/TAZ are predominantly expressed in RG/APs, whereas
117 TEAD1 is expressed in both RG and IPs (including SAPs and BPs).
118

119 **YAP/TAZ loss and TEAD1/2 loss result in different defects in the subpallium**

120 The above finding led us to hypothesize that TEAD may act independent of YAP/TAZ in IPs
121 during telencephalon development. To test this, we decided to compare the phenotypes of
122 genetic mutants lacking *Yap* and *Taz* (*Yap;Taz*) to those lacking *Tead*. Besides *Tead1*, *Tead2*
123 mRNA is also detected in the VZ/SVZ throughout the developing CNS[29] (Supplementary Fig.
124 1a). *Tead3* transcript levels in the telencephalon are very low (Supplementary Fig. 1a). Our
125 RNA-sequencing (RNA-seq) data suggest that *Tead4* is not expressed in the developing CNS
126 (data not shown). Therefore, we generated *Yap;Taz* double conditional knockout (dKO),
127 *Tead1;2* dKO, and *Tead1* and *Tead2* single conditional KO (cKO) mice using a *Nestin-Cre* line,
128 which is expressed in the developing CNS starting from around embryonic day (E) 10.5. The
129 depletion of corresponding proteins was validated by Western blot (Supplementary Fig. 1b).
130 Both *Yap;Taz* dKO and *Tead1;2* dKO mice died soon after birth. Therefore, we collected
131 E17.5 brains for histological analysis. Obvious defects were observed in both mutants. In the
132 subpallium, both mutants showed structural disruption of the VS and disorganization of the VZ-
133 SVZ (Fig. 1d, arrows); similar defects were also present in the cortex of *Yap;Taz* dKO mice

134 when *Yap;Taz* were deleted with *Emx1-Cre*[13]. Interestingly, *Tead1;2* dKO, but not *Yap;Taz*
135 dKO, mice showed a marked expansion of ASCL1$^+$ cells (Fig. 1d), suggesting that TEAD1/2
136 have YAP/TAZ-independent functions during subpallial development. Cortical neural
137 progenitors, labeled by SOX2 and TBR2, were notably reduced in *Yap;Taz* dKO mice
138 (Supplementary Fig. 1c), consistent with our previous report when *Yap;Taz* were deleted with
139 *Emx1-Cre*[13]. This phenotype, however, was not present in *Tead1;2* dKO mice, suggesting either
140 that TEAD1/2 are not required in cortical progenitors or that the loss of *Tead1;2* is compensated
141 by other genes. Here we focused on investigating the role of TEAD1/2 during subpallial
142 development.
143 The telencephalon of *Tead1* and *Tead2* single cKO mice did not show obvious defects at
144 E17.5 (Supplementary Fig. 1d). However, *Tead1* cKO mice exhibited hydrocephaly postnatally
145 (Supplementary Fig. 1d) and all died within 3 weeks of age. *Tead2* cKO mice did not show
146 gross defects in brain development and were healthy and fertile. These results suggest that,
147 functionally, *Tead1* and *Tead2* are largely redundant during brain development, although *Tead1*
148 is probably more important than *Tead2*.
149

150 **TEAD1/2 loss and YAP/TAZ loss similarly disrupt subpallial apical junctions**

151 The disruptions in the subpallial VS of E17.5 *Tead1;2* dKO and *Yap;Taz* dKO mice suggested
152 defects in the apical junctions that support neuroepithelial structural integrity. Indeed,
153 immunostaining using apical junction markers ZO-1, β-catenin, and aPKC revealed disruptions
154 in these junctions as early as E13.5 in both dKO lines (Supplementary Fig. 2, arrows), indicating
155 that TEAD1/2 and YAP/TAZ are both required to maintain the integrity of neuroepithelial apical
156 junctions.
157

158 **TEAD1/2 loss and YAP/TAZ loss have distinct impact on lineage progression of**
159 **subpallial neural progenitors**

160 To pinpoint which progenitor subtypes/states were affected upon TEAD1/2 loss and YAP/TAZ
161 loss, we focused our analyses on the MGE. Previous studies have shown that nearly all cells in
162 the VZ of MGE express OLIG2 as early as E10.5[27], and that ASCL is expressed in cells both in
163 the VZ and the SVZ[26-28]. Studies have also found that the manner in which ASCL1 is expressed
164 has distinct impact on cell fate; oscillatory expression maintains progenitor proliferation and self-
165 renewal, whereas sustained expression promotes neuronal commitment and differentiation[30].
166 We performed OLIG2, ASCL1, and pH3 triple immunostaining to correlate OLIG2 and ASCL1

167 expression patterns with progenitor subtype (Fig. 2a). Quantification suggested that nearly all
168 OLIG2^{+}ASCL1^{-} cells were APs; that among OLIG2^{+}ASCL1^{+} cells, ~40% were APs, ~50% were
169 SAPs, and ~10% were BPs; that nearly all OLIG2^{-}ASCL1^{+} and OLIG2^{-}ASCL1^{-} progenitor cells
170 were BPs (Fig. 2b). From another perspective: APs were composed of OLIG2^{+}ASCL1^{-} (~60%)
171 and OLIG2^{+}ASCL1^{+} (~40%) cells; nearly all SAPs were OLIG2^{+}ASCL1^{+} cells, and BPs were
172 composed of roughly equal fractions of OLIG2^{+}ASCL1^{+}, OLIG2^{-}ASCL1^{+}, and OLIG2^{-}ASCL1^{-}
173 (and presumably Ki67^{+}) cells (Fig. 2c). Taken together, we propose that MGE neural
174 progenitors oscillate between the OLIG2^{+}ASCL1^{-} and OLIG2^{+}ASCL1^{+} states, then—upon
175 neuronal commitment—progress from the OLIG2^{+}ASCL1^{+} state to the OLIG2^{-}ASCL1^{+} state,
176 and finally to the OLIG2^{-}ASCL1^{-} state (Fig. 2d). Although defining progenitor states in this
177 manner is not ideal, as the OLIG2^{+}ASCL1^{+} state contains cells in different cell states and some
178 are probably no different from cells in the OLIG2^{+}ASCL1^{-} state, this approach at least allows us
179 to distinguish early progenitors (OLIG2^{+}ASCL1^{-} and OLIG2^{+}ASCL1^{+}) and late progenitors
180 (OLIG2^{-}ASCL1^{+} and OLIG2^{-}ASCL1^{-}).
181 Next, we quantified the number of progenitors in each of the states defined above; the
182 proliferation marker Ki67 was used as a generic marker for progenitor cells (Fig. 2e). In *Tead1;2*
183 dKO MGE, OLIG2^{+}ASCL1^{+} progenitors were significantly increased at E13.5 and E14.5
184 compared to control MGE while OLIG2^{-}ASCL1^{-} progenitors significantly decreased at E14.5. In
185 contrast, in *Yap;Taz* dKO MGE, OLIG2^{+}ASCL1^{+} progenitors were significantly decreased at
186 E13.5 and E14.5 while OLIG2^{-}ASCL1^{+} and OLIG2^{-}ASCL1^{-} progenitors significantly increased
187 at E14.5. In both dKO lines, the numbers of OLIG2^{+}ASCL1^{-} cells were not significantly changed
188 (Fig. 2e). Thus, TEAD1/2 loss and YAP/TAZ loss have distinct impacts on the lineage
189 progression of subpallial progenitors: TEAD1/2 loss expands the early progenitor
190 (OLIG2^{+}ASCL1^{+}) population, whereas YAP/TAZ loss depletes early progenitors and expands
191 late (OLIG2^{-}) progenitors.
192
193 **TEAD1/2 loss and YAP/TAZ loss differentially affect MGE cellular output**

194 MGE progenitors give rise to cortical interneurons, projection neurons and interneurons in the
195 basal ganglia, and OLCs in the embryonic cortex[4,31,32]., In *Tead1;2* dKO mice, the percentage of
196 TUJ1$^+$ area within the MGE and the number of MAFB$^+$ immature interneurons[33] in the neocortex
197 were significantly reduced at E14.5 compared to those in control mice (Fig. 3). Cortical OLCs
198 labeled by OLIG2 and SOX10[34] were also significantly reduced in *Tead1;2* dKO mice at E17.5
199 (Fig. 3). These results suggest that TEAD1/2 loss impairs the production of neurons and OLCs
200 by the MGE.

201 In *Yap;Taz* dKO mice, the percentage of TUJ1$^+$ area within the MGE was increased at
202 E14.5 compared to control mice, although the number of MAFB$^+$ immature interneurons in the
203 neocortex was unchanged (Fig. 3). Cortical OLCs were increased in *Yap;Taz* dKO mice at
204 E17.5; intriguingly, many OLIG2- and SOX10-labeled cells were found along cortical VS in
205 *Yap;Taz* dKO (Fig. 3, arrowheads), which were rarely seen in control mice. These results
206 suggest that YAP/TAZ loss causes premature neuronal differentiation. Whether YAP/TAZ loss
207 enhances OLC differentiation by MGE progenitors remains to be determined because it is
208 unclear whether the excess OLCs found *Yap;Taz* dKO cortices were derived from MGE or
209 cortical progenitors. Taken together, our results demonstrate that TEAD1/2 loss and YAP/TAZ
210 loss differentially affect the cellular output from MGE neural progenitors.
211

212 **Single-cell RNA-seq analysis reveals distinct impacts of TEAD1/2 loss and**
213 **YAP/TAZ loss on MGE neural progenitor lineage progression**

214 To confirm the changes in MGE progenitor population in our mutant mice and to hopefully better
215 define progenitor states, we performed single-cell RNA-seq (scRNA-seq) using microdissected
216 MGE from E14.5 *Tead1;2* dKO, *Yap;Taz* dKO, and their corresponding no-*Cre* littermate
217 controls, as well as MGE from E12.5 and E15.5 wild-type (WT) mice.

218 To understand MGE lineage progression during normal development, we first analyzed
219 WT cells, which included E12.5 and E15.5 WT cells and E14.5 *Tead1;2* control cells. We
220 clustered them based on highly variable genes (HVGs) and visualized them by uniform manifold
221 approximation and projection (UMAP) (Fig. 4a and Supplementary Fig. 3a). To annotate the cell
222 clusters, we compiled a list of progenitor genes and a list of neuron genes (Supplementary data
223 1) based on previous publications[32,35] and scored each cell based on their expression of these
224 genes. This analysis indicated that clusters 2, 3, and 6 were predominantly composed of
225 progenitor cells and clusters 1, 4, 5, 7, and 8 were composed of neurons (Fig. 4a–c). This
226 conclusion is supported by cell-cycle phase analysis, which showed that cells in clusters 2, 3,

227 and 6 were predominantly proliferating cells in S and G2/M phases, and cells in clusters 1, 4, 5,
228 7, and 8 were postmitotic cells in G1/G0 phases (Fig. 4d). Based on marker gene expression,
229 cells in cluster 9 were endothelial cells (*Igfbp7*), in cluster 10 were red blood cells (*hba* and
230 *hbb*), and in cluster 11 were microglia (*Cx3cr1*).

231 Next, we subset out the progenitor clusters (clusters 2, 3, and 6) for further analysis.
232 When HVGs were used for feature selection, progenitor cells were organized largely based on
233 their cell-cycle phase; for example, cluster 3 was mostly composed of S-phase cells and cluster
234 6 was composed of G2/M-phase cells (Fig. 4d). A previous study of subpallial development has
235 found that clustering cells using transcription factors mitigates the influence of cell-cycle phase
236 and improves resolution of developmental populations[36]. We adopted this approach and
237 compiled a list of 742 transcription factor genes (Supplementary data 1) based on both the
238 aforementioned study and the Allen Developing Mouse Brain Atlas RNA in situ hybridization
239 data[37]. Using this list for feature selection, cells in different cell-cycle phases intermingled when
240 visualized by UMAP (Fig. 4e), indicating that the influence of cell-cycle phase was largely
241 abolished. Scoring the cells using our curated lists of genes enriched in the VZ and in the SVZ
242 and mantle zone (SVZ-MZ) (Supplementary data 1 and Supplementary Fig. 3b) showed a
243 gradual, unidirectional transition of VZ and SVZ-MZ scores on UMAP (Fig. 4f, g). Pseudotime
244 analysis by Monocle 3 also revealed a gradual, unidirectional transition (Fig. 4h). Together,
245 these results suggest that using our list of transcription factors to cluster MGE progenitor cells is
246 able to capture their lineage progression.

247 How many MGE progenitor states/subtypes are there? To address this question, we
248 used an unbiased, systematic approach by stepwise (0.025) increasing the clustering resolution
249 and plotting the results in a “cluster tree” (Supplementary Fig. 3c). When the resolution was less
250 than 0.25, cells often changed their cluster membership at the next resolution (Supplementary
251 Fig. 3c, grey diagonal arrows), suggesting that the clusters were unstable. When the resolution
252 was 0.25 and higher, however, cells no longer changed their cluster membership other than
253 splitting into smaller clusters (Supplementary Fig. 3c). We therefore concluded that 0.25 was the
254 optimal resolution, yielding 4 clusters with comparable size, which we referred to as progenitor
255 state (PS) 1 to PS4 with PS1 being the earliest progenitor state and PS4 being the latest (Fig.
256 4i). Expression counts of *Olig2* were high in PS1 and PS2 and low in PS3 and PS4, whereas
257 that of *Ascl1* were low in PS1, high in PS2 and PS3, and medium in PS4 (Fig. 4j). These results
258 match well with the progenitor states defined by OLIG2 and ASCL1 immunostaining (Fig. 2d),
259 validating our computational methods to analyze and annotate MGE progenitor cells.

260 Next, we combined WT, *Tead1;2* dKO, *Yap;Taz* dKO, and no-*Cre* controls cells,
261 clustered them based on HVGs (Fig. 4k and Supplementary Fig. 3d), and identified progenitor
262 clusters—clusters 2, 3, and 5—based on progenitor/neuron scoring and cell-cycle phase
263 analysis (Fig. 4l–n). We then assigned progenitor states by using the annotation of WT
264 progenitor cells as the reference[38] (Fig. 4o, Supplementary Fig. 3e). To compare the distribution
265 of progenitor cells in each progenitor state between control and dKO samples, we used
266 *propeller*, a method for testing for differences in cell type proportions in scRNA-seq data[39]. In
267 *Tead1;2* dKO samples, the proportion of progenitor cells in PS2 was significantly increased and
268 the proportions in PS3 and PS4 significantly decreased compared to control. In contrast, in
269 *Yap;Taz* dKO samples, the proportion of progenitor cells in PS1 was significantly decreased and
270 the proportion in PS4 significantly increased (Fig. 4p). These results correlate well with that
271 obtained by immunostaining (Fig. 2e); both approaches find that TEAD1/2 loss expands the
272 early progenitor population and depletes later progenitors, whereas YAP/TAZ loss has the
273 opposite effect—it depletes early progenitors and expands late progenitors. Pseudotime
274 analysis further supports this conclusion (Supplementary Fig. 3f).
275

276 TEAD1/2 loss impedes developmental progression of subpallial neural 277 progenitors

278 The consequence of YAP/TAZ loss in the subpallium, a depletion of early progenitors, is
279 consistent with the known function of YAP/TAZ in promoting the proliferation and self-renewal of
280 diverse types of stem/progenitor cells[11,12]. However, that TEAD1/2 loss results in an expansion
281 of early progenitors is unexpected. Therefore, we investigated the cellular mechanism driving
282 this expansion.
283 A faster cell-cycle speed could lead to increased cell numbers within a given time
284 window. We measured cell-cycle speed using a sequential EdU-BrdU labeling method[40]. The
285 cell-cycle length and the S-phase length of OLIG2^{+}ASCL1^{+} cells—the population expanded in
286 *Tead1;2* dKO MGE—and of OLIG2^{+}ASCL1^{-} cells were significantly increased in *Tead1;2* dKO
287 MGE compared to control (Fig. 5a), indicating a slowing down of cycling speed. This could not
288 explain why the number of OLIG2^{+}ASCL1^{+} cells was increased in *Tead1;2* dKO MGE.
289 Next, we tested whether the developmental progression of early progenitors was stalled
290 in *Tead1;2* dKO MGE. To this end, we performed lineage tracing by injecting FlashTag into the
291 cerebral ventricles of E12.5 embryos in utero to pulse label M-phase APs[41] and monitoring the
292 fate of labeled cells 12, 24, and 48 h post injection (hpi). At 12 and 24 hpi, the fate of FlashTag-

293 labeled cells in control and *Tead1;2* dKO MGE was similar (Fig. 5b); in both genotypes the
294 fractions of labeled cells existing in early progenitor (OLIG2^{+}) states decreased while those
295 adopting later progenitor (OLIG2^{-}) states increased comparing 24 hpi vs. 12 hpi (Fig. 5b),
296 consistent with developmental progression. At 48 hpi, however, significantly larger fractions of
297 labeled cells remained in the OLIG2^{+} early progenitor states—especially the OLIG2^{+}ASCL1^{+}
298 state—rather than progressing to the OLIG2^{-} late progenitor states in *Tead1;2* dKO than in
299 control MGE (Fig. 5b). Thus, TEAD1/2 promote developmental progression of subpallial neural
300 progenitors; their loss stalls the cells in early progenitor states.
301

302 **TEAD1/2 promote lineage progression of subpallial progenitors by inhibiting**
303 **Notch signaling**

304 To uncover the molecular mechanism underlying the expansion of early progenitors in *Tead1;2*
305 dKO MGE, we exploited our scRNA-seq dataset and performed differential expression analysis
306 using scMINER[42] and gene set enrichment analysis (GSEA) using NetBID2[43], comparing
307 *Tead1;2* dKO and control PS2 cells, the progenitor state that was expanded in *Tead1;2* dKO
308 MGE (Supplementary data 2). Several signaling pathway gene sets in the Hallmark collection
309 were significantly upregulated in *Tead1;2* dKO PS2 cells, among which Notch_signaling was
310 upregulated the most strongly (Fig. 6a, b). Interestingly, several cell cycle related gene sets,
311 such as E2F_targets and G2M_checkpoint, were significantly downregulated in *Tead1;2* dKO
312 PS2 cells (Fig. 6a and Supplementary data 2), which is consistent with our finding that the cell-
313 cycle speed of early progenitor cells was slowed down in *Tead1;2* dKO MEG.
314 Notch signaling is a key regulator of neural progenitor cells. Both *Notch1* and *Notch3*
315 regulate lineage progression of subpallial neural progenitors, with *Notch1* being the more
316 important paralog. Conditional deletion of *Notch1* leads to accumulation of *Ascl1*-expressing
317 cells in the subpallial VZ-SVZ boundary while depleting *Ascl1*-expressing cells in the SVZ[44], a
318 phenotype that is, to an extent, opposite to that of *Tead1;2* dKO mice. *Notch1-3* and Notch
319 target genes *Hes1* and *Hes5* were all significantly upregulated in *Tead1;2* dKO PS2 cells
320 compared to control PS2 cells (Fig. 6c and Supplementary data 2). We confirmed the
321 upregulation of *Notch1* and *Hes5*—the most highly expressed *Notch* and *Hes* genes in PS2
322 cells—by RNAscope (Fig. 6d).
323 To determine whether upregulation of Notch signaling contributes to the expansion of
324 early progenitors in *Tead1;2* dKO mice, we performed genetic rescue experiments by deleting
325 one allele of *Notch1* in the *Tead1;2* dKO background. This, unfortunately, did not rescue the

326 subpallial phenotype of *Tead1;2* dKO mice (data not shown). We reasoned that the failure of
327 rescue was probably because the phenotype of *Tead1;2* dKO mice was too severe. Therefore,
328 we attempted the rescue in the *Tead1*$^{F/F}$*;Tead2*$^{F/+}$*;Nestin-Cre* background; these mice also
329 exhibited consistent expansion of the ASCL1^{+} progenitor population at postnatal day (P) 0 (Fig.
330 6e, f), although not as severely as *Tead1;2* dKO mice did. Loss of one allele of *Notch1*, which
331 had no effect on the number of ASCL1^{+} cells in the WT background, completely restored the
332 number of ASCL1^{+} cells in *Tead1*$^{F/F}$*;Tead2*$^{F/+}$*;Nestin-Cre* mice to the control level (Fig. 6e, f).
333 These results indicate that TEAD1/2 promote lineage progression of subpallial neural
334 progenitors at least in part by inhibiting Notch signaling. Note that in *Tead1*$^{F/F}$*;Tead2*$^{F/+}$*;Nestin-*
335 *Cre* subpallium, the VS, apical junctions, and VZ-SVZ organization were disrupted (Fig. 6e,
336 arrows and insets), just like in *Tead1;2* dKO mice. These defects, however, were not rescued by
337 the loss of one allele of *Notch1* (Fig. 6e, arrows and insets), suggesting that upregulation of
338 Notch signaling is not responsible for these defects.
339

340 **TEAD1/2 act with INSM1 to promote lineage progression of subpallial neural**
341 **progenitors**

342 The distinct subpallial phenotypes of *Tead1;2* dKO and *Yap;Taz* dKO mice strongly suggest that
343 TEAD1/2 regulate lineage progression of subpallial neural progenitors independent of YAP/TAZ.
344 In addition to Yorki/YAP/TAZ, Scalloped/TEAD interacts with Vestigial/VGLL1–3[19,20],
345 Tgi/VGLL4[45,46], Nerfin-1/INSM1[47,48], and RUNX2/3[49,50], among which only *Vgll4* (*Vestigial like 4*)
346 and *Insm1* are expressed in subpallial progenitor cells (Supplementary Fig. 4a). By competing
347 with YAP/TAZ for TEAD binding, VGLL4-mediated transcriptional repression antagonizes
348 YAP/TAZ-mediated transcriptional activation of TEAD target genes[51,52]. To test whether
349 TEAD1/2 act with VGLL4 to regulate subpallial lineage progression, we generated *Vgll4* null
350 mice and *Nestin-Cre*–mediated cKO mice. Null mice all died before P7 (Supplementary Fig. 4b),
351 an outcome reported previously[53]. However, cKO mice did not exhibit any obvious brain
352 development phenotype (Supplementary Fig. 4d), suggesting that VGLL4 is not an important
353 cofactor for TEAD in the context of subpallial development.
354 INSM1 is a zinc-finger transcription factor with an N-terminal SNAG (Snail/Gfi-1) domain
355 that interacts with transcriptional corepressors such as KDM1A/LSD1 (lysine (K)-specific
356 demethylase 1A)[54]. *Insm1* mRNA is expressed in neural progenitors and nascent neurons
357 throughout embryonic and adult neurogenesis[55]. Within neural progenitors, *Insm1* is expressed
358 in non-surface dividing SAPs and BPs but not in APs[55-57]. Previous studies have found that

359 *Insm1* deletion leads to increased subpallial VZ/SVZ size and the number of Ki67$^+$ cells and
360 decreased embryonic cortical OLCs[56,58]—similar to the effects of *Tead1;2* deletion, raising the
361 possibility that TEAD1/2 act with INSM1 to regulate subpallial development. To test this, we
362 examined INSM1 expression pattern in the MGE (Fig. 7a). At E12.5, INSM1 was expressed in
363 some VZ cells and more frequently in SVZ cells. All INSM1$^+$ cells in the VZ and a subset of
364 INSM1$^+$ cells in the SVZ, especially those close to the VZ, also expressed TEAD1.
365 We validated TEAD-INSM1 interaction by co-immunoprecipitation using transfected
366 HEK293T cells (Fig. 7b). Proximity ligation assay (PLA) using E12.5 brain sections further
367 confirmed TEAD-INSM1 interaction in the subpallium (Fig. 7c). Interestingly, whereas the PLA-
368 detected interactions (PLA$^+$ spots) between TEAD1 and YAP were enriched near the ventricular
369 surface, the interactions between TEAD1 and INSM1 were more frequent near the VZ-SVZ
370 boundary (Fig. 7c).
371 Previous characterizations of *Insm1* KO mice did not define the affected progenitor
372 subtype/state with molecular markers. Therefore, we generated *Insm1* cKO mice using *Nestin-*
373 *Cre*; the loss of INSM1 protein was confirmed by Western blot (Supplementary Fig. 5a). The
374 OLIG2$^+$ASCL1$^+$ progenitor population was significantly expanded and the OLIG2$^-$ASCL1$^-$
375 population significantly decreased in *Insm1* cKO mice at E14.5 (Fig. 7d, e). The ASCL1$^+$
376 population remained expanded at P0 (Supplementary Fig. 5c). These phenotypes recapitulate
377 that of *Tead1;2* dKO mice, supporting the hypothesis that TEAD1/2 and INSM1 act together to
378 promote lineage progression of subpallial neural progenitors. A notable phenotypic difference
379 between *Tead1;2* dKO and *Insm1* cKO subpallium is that the VS, apical junctions, and VZ-SVZ
380 organization were not disrupted in *Insm1* cKO mice (Fig. 7d and Supplementary Fig. 5b), unlike
381 in *Tead1;2* dKO mice; this is consistent with the idea that TEAD1/2 act with YAP/TAZ to
382 maintain the integrity of neuroepithelial apical junctions.
383

384 ## Discussion

385 The mechanisms governing lineage progression of subpallial neural progenitor cells are poorly
386 understood. In this study, we discovered that the TEAD family of transcription factors promotes
387 lineage progression of subpallial neural progenitors. Importantly, this function of TEAD is
388 independent of its best-known cofactors, YAP/TAZ, the key effectors of the Hippo pathway.
389 Instead, we suggest that TEAD acts with INSM1 in this developmental context.

390 Prompted by the hypothesis that TEAD may have YAP/TAZ-independent functions
391 during vertebrate neural tube development, we compared conditional mouse mutants lacking
392 *Tead1* and *Tead2* (*Tead1;2* dKO) to those lacking *Yap* and *Taz* (*Yap;Taz* dKO). The distinct,
393 essentially opposite, phenotype in the subpallium of these two mutant lines confirms our
394 hypothesis. YAP/TAZ loss results in decreased numbers of subpallial early progenitors and
395 increased numbers of late progenitors and neurons, indicative of reduced early progenitor self-
396 renewal and premature differentiation, which is consistent with the well-established function of
397 YAP/TAZ in promoting stem/progenitor cell self-renewal. In striking contrast, TEAD1/2 loss
398 results in an expansion of early progenitors and reduction in late progenitors, neurons, and
399 OLCs, suggesting that TEAD1/2 promote developmental progression of subpallial neural
400 progenitors. One phenotype, however, is present in both mutant lines: the disruption of
401 subpallial VS and VZ-SVZ organization, likely caused by defects in neuroepithelial apical
402 junctions. We have shown that YAP/TAZ regulate the expression of cell junction genes in
403 cortical neural progenitors[13]; the shared junctional defect suggests that YAP/TAZ and TEAD act
404 together to regulate these genes. Taken together, our study demonstrates that, during
405 mammalian subpallial development, TEAD has both YAP/TAZ-dependent and -independent
406 functions.
407 Interestingly, despite having similar expression patterns in cortical and subpallial neural
408 progenitors, TEAD1/2 loss specifically perturbs subpallial, but not cortical, development. It is
409 unclear whether TEAD function is uniquely required in subpallial progenitors, or whether *Tead3*
410 and/or *Tead4* compensate for the loss of *Tead1*;*2* in cortical progenitors. In comparison,
411 YAP/TAZ loss affects the structural organization and self-renewal of cortical and subpallial
412 progenitors similarly. Furthermore, in addition to having fewer early neural progenitors and more
413 late progenitors and neurons in the MGE, *Yap;Taz* dKO embryos had more OLCs in the cortex.
414 Interestingly, many OLCs were found along the VS in *Yap;Taz* dKO cortices, which rarely
415 occurs in control embryos. Because cortical progenitors lacking YAP/TAZ are defective in their
416 self-renewal and proliferation capacities[13], it is possible that the OLCs located at VS were
417 derived from cortical progenitors as a result of their abnormal differentiation, rather than from
418 subpallial progenitors; resolving this will require future experiments using cortical and MGE
419 region-specific *Yap;Taz* mutants.
420 Unlike in the cortex where RG/APs and IPs/BPs are readily distinguished by
421 immunostaining (e.g., RG are $SOX2^{+}TBR2^{-}$ and IPs are $TBR2^{+}$), progenitor subtype/state in
422 the subpallium has not been defined in a similar manner. We used the combined immunosignals
423 of OLIG2 and ASCL1—because their expression patterns are well characterized and because

424 excellent antibodies are available—and defined four subpallial progenitor states. Although these
425 progenitor states likely reflect the lineage progression of subpallial progenitors and, importantly,
426 allowed us to distinguish early vs. late progenitors, there are several weaknesses with this
427 approach. First, the four progenitor states do not progress in a linear fashion; cells in the
428 OLIG2^{+}ASCL1^{-} state oscillate with a subset of cells in the OLIG2^{+}ASCL1^{+}state due to the
429 oscillatory expression of ASCL1[30]. Second, the OLIG2^{+}ASCL1^{+} state contains several subtypes
430 of progenitors (APs/RG, SAPs, and BPs). Lastly, this approach does not distinguish RG and
431 IPs. Therefore, although our analysis shows that the OLIG2^{+}ASCL1^{+} early progenitor population
432 is affected—increased in *Tead1;2* dKO mice and decreased in *Yap;Taz* dKO mice, it remains
433 unclear whether RG/APs, SAPs, or BPs are affected; using mitotic location to distinguish them
434 is not feasible due to the disorganization of VZ-SVZ in both mutant lines.
435 To complement immunohistological analysis and overcome at least some of the
436 weaknesses mentioned above, we employed scRNA-seq to characterize our mutant lines
437 because this approach offers a more comprehensive view of cell state by measuring the
438 expression levels of thousands of genes. Previous scRNA-seq analyses of the developing
439 mouse subpallium did not define progenitor states in detail[32,35,59]. By using a curated list of 742
440 transcription factors for feature selection and using stepwise increase of clustering resolution to
441 identify the optimal cluster number, we defined four MGE progenitor states. Based on marker
442 gene expression (*Olig2* and *Ascl1*), the four progenitor states defined by scRNA-seq—or more
443 precisely, by the expression of the 742 transcription factors—correlate well with the four
444 immunostaining-defined states. However, the progenitor states defined by these two methods
445 are not identical. For example, in WT E14.5 MGE, the OLIG2^{+}ASCL1^{+} state contains about
446 twice the number of cells than the other states do, whereas the four progenitor states defined by
447 scRNA-seq are of comparable size, with the third state (PS3) being the largest. More
448 importantly, both gene signature analysis using VZ and SVZ-MZ gene scores and pseudotime
449 analysis showed gradual, unidirectional transition of scRNA-defined progenitor states, rather
450 than the oscillatory behavior between the two early progenitor states defined by
451 immunostaining. Given that scRNA-based analysis takes into account much richer information
452 and is much less biased than immunostaining-based analysis (which is limited by antibody
453 availability and influenced by definition of immunosignal positivity), it is likely that the progenitor
454 states defined by scRNA-seq reflect more accurately the true states and transition of progenitor
455 cells during development. Our scRNA-seq analysis probably detected at least some of the
456 different states of OLIG2^{+}ASCL1^{+} cells—perhaps those in the self-renewal state (that oscillate

457 with the OLIG2^{+}ASCL1^{-} state) vs. those committed to differentiation—and separated them into
458 two progenitor states, PS1 and PS2, respectively. Interestingly, our scRNA-seq analysis found
459 that YAP/TAZ loss and TEAD1/2 loss affect different early progenitor states: YAP/TAZ loss
460 reduces PS1, whereas TEAD1/2 loss expands PS2. This insight is not obtained from
461 immunohistological analysis, likely due to the heterogeneity of the OLIG2^{+}ASCL1^{+} state. That
462 YAP/TAZ loss reduces PS1 is consistent with YAP/TAZ being predominantly expressed in APs
463 and suggests that YAP/TAZ promote AP self-renewal and/or proliferation. Whether YAP/TAZ
464 require TEAD for this function is unclear, as the absence of a reduction in PS1 in *Tead1;2* dKO
465 mice could have been masked by the expansion of PS2 due to certain feedback or homeostasis
466 mechanism; compensation by *Tead3* or *Tead4* is unlikely because they were not upregulated in
467 *Tead1;2* dKO PS1 cells (data not shown).
468 It is likely that TEAD loss and YAP/TAZ loss affect not only the number of cells
469 belonging to a progenitor state but also the cell state (of the general sense) itself. In our "cluster
470 tree" analysis, *Tead1;2* dKO progenitor cells switched between clusters upon a small change in
471 clustering resolution more readily than WT progenitor cells did (data not shown), suggesting that
472 the cell states of *Tead1;2* dKO cells are less well defined than that of WT cells. Furthermore,
473 differential expression and GSEA analyses comparing dKO and control cells of the same
474 progenitor state revealed many significantly changed gene sets (Supplementary data 2 and data
475 not shown), indicative of different biological activities—which constitute a cell state—between
476 dKO and control cells in the same progenitor state. This type of analyses led us to discover that
477 TEAD promotes subpallial progenitor lineage progression at least in part by inhibiting Notch
478 signaling.
479 Based on the co-expression and physical interaction between TEAD and INSM1 in the
480 subpallium and the phenotypic similarity between their mutants—both showed expansion of the
481 OLIG2^{+}ASCL1^{+} population, we suggest that TEAD acts with INSM1 to promote subpallial
482 progenitor lineage progression. The physical interaction between orthologs of TEAD and INSM1
483 is evolutionarily conserved[22,47,48]. Our study demonstrates that the function of this transcription
484 factor complex in regulating neurogenesis is also conserved. In *C. elegans*, this complex (EGL-
485 44 and EGL-46) instructs cell cycle exit during the lineage progression of a specific neuroblast[22]
486 and controls neuronal cell fate in specific neurons[21]. In *Drosophila*, this complex (Scalloped and
487 Nerfin-1) maintains specific neuronal fate; in its absence, terminally differentiated medulla
488 neurons in the optic lobes revert back to a neuroblast-like state[47]. Interestingly, Scalloped and
489 Nerfin-1 maintains medullar neuron fate at least in part by repressing Notch signaling, which

490 echoes our finding that TEAD1/2 promote subpallial progenitor lineage progression also by, at
491 least in part, inhibiting Notch signaling. In both *C. elegans* and *Drosophila*, orthologs of TEAD
492 and INSM1 only act together in specific contexts, while both playing additional roles
493 independent of the other. During mammalian neural development, INSM1 has been shown to
494 promote the generation and expansion of BPs in the cortex[56], specify monoaminergic neuronal
495 phenotypes in the hindbrain[60], control the development of pituitary endocrine cells[54], and
496 consolidate outer hair cell fate in the cochlea[61]. It remains to be determined whether INSM1
497 functions with TEAD in any of these contexts.
498 In summary, we propose that during subpallial development, TEAD interacts with
499 different partners in different progenitor subtypes/states to execute distinct functions (Fig. 8). In
500 APs, TEAD interacts with YAP/TAZ to maintain neuroepithelial structural integrity; whether
501 TEAD also promotes self-renewal and proliferation with YAP/TAZ remains to be determined. In
502 SAPs and possibly a subset of BPs, TEAD interacts with INSM1 to promote lineage progression
503 at least in part by inhibiting Notch signaling.
504

505 # Methods

506 ## Mice

507 The *Nestin-Cre* line[62] (#003771) and *Notch1*^{F} allele[63] (#007181) was purchased from the
508 Jackson Laboratory (JAX). *Tead2*$^{F/F}$ mice[64], *Yap*$^{F/F}$*;Taz*$^{F/F}$ mice[65], and *Insm1*$^{F/F}$ mice[61] were
509 kindly provided by Drs. Melvin DePamphilis, Eric Olson, and Jaime García-Añoveros,
510 respectively. To generate the *Tead1*^{F} allele, *Tead1*^{tm1a} (#050015-UCD) was obtained from
511 Mutant Mouse Resource & Research Centers UC Davis (MMRRC-UCD) and crossed with a
512 ubiquitous *Rosa26-FLP* line (JAX #016226). Both *Tead1* and *Tead2* are on chromosome 7. A
513 recombined chromosome 7 harboring both *Tead1*^{F} and *Tead2*^{F} alleles was generated by
514 crossing *Tead1*$^{F/+}$*;Tead2*$^{F/+}$ trans-heterozygous mice with wild-type mice and screening for
515 progenies carrying both *Tead1*^{F} and *Tead2*^{F} alleles. Two *Vgll4*^{F} lines were generated by using
516 CRISPR-Cas9–mediated gene editing to insert two *loxP* sites flanking exon 2 in one line and
517 exon 3 in the other. The corresponding deleted alleles (*Vgll4*$^{\Delta}$) were generated by crossing
518 *Vgll4*$^{F/F}$ mice with *Sox2-Cre* (JAX #008454) females, which express *Cre* in their germline. All
519 mice were maintained in a mixed genetic background. All animal procedures were approved by
520 the Institutional Animal Care and Use Committee of St. Jude Children's Research Hospital.
521

522 ## Histology, immunostaining, and image acquisition

523 Mouse brains were dissected in cold PBS, fixed overnight in 4% paraformaldehyde at 4°C, and
524 washed in PBS. For paraffin sections, fixed brains were dehydrated in 70% ethanol overnight,
525 embedded in paraffin, and sectioned at 5-μm thickness. For histological analysis, sections
526 were rehydrated and stained with hematoxylin and eosin (H&E) or Luxol blue and Nissl. For
527 frozen sections, fixed brains were cryoprotected in 30% sucrose overnight at 4°C, embedded in
528 Tissue Freezing Medium (Thermo Scientific), and sectioned at 12–20-μm thickness. For
529 immunostaining, sections were washed twice in PBS, blocked and permeabilized in PBS with
530 3% normal donkey serum and 0.2% Triton X-100 for 1 h, and incubated with primary
531 antibodies at 4°C overnight. Sections were then washed in PBS 3 times and incubated with
532 appropriate fluorescence–conjugated secondary antibodies (Jackson ImmunoResearch
533 Laboratories or Thermo Scientific Invitrogen) at 1:1000 dilution and DAPI (1:1000 dilution) for
534 2–3 h at room temperature. After 3 washes in PBS, sections were coverslipped in ProLong
535 Gold (Thermo Scientific Invitrogen #P36930). The following primary antibodies were used:
536 Alexa Fluor 647-Sox2 (BD Biosciences, #562139, 1:100), BrdU (Abcam ab6326, 1:100), β-
537 catenin (BD Biosciences #610153, 1:500), TBR2/EOMES (eBioscience, #14-4875, 1:100),
538 phospho-Histone H3 (Ser10) (Cell Signaling Technologies (CST) #9706, 1:500), INSM1 (Santa
539 Cruz Biotechnologies sc-271408 AF488, 1:50), Ki67 (Invitrogen #14-5698-82, 1:1000), MAFB
540 (Sigma HPA005653, 1:500), ASCL1 (Abcam ab211327, 1:500), PKCζ/aPKC (Santa Cruz sc-
541 216, 1:1000), SOX10 (Santa Cruz sc-17342, 1:250), OLIG2 (R&D, af2418, 1:250), TEAD1 (CST
542 #12292, 1:250), TUJ1 (BioLegend #801202, 1:100), YAP/TAZ (CST #8418, 1:500), and ZO-1
543 (Invitrogen #339188, 1:500).
544 Images of H&E- or Luxol blue/Nissl-stained sections were acquired using a Zeiss Stereo
545 Discovery V8 microscope equipped with an AxiocamMRc camera and processed with
546 Axiovision. Low magnification fluorescent images were acquired using an Olympus BX63
547 microscope equipped with an Orca Flash4.0 camera. High magnification fluorescent images
548 were acquired using a Zeiss LSM 780 confocal or a Zeiss Apotome microscope.
549

550 **Image Quantifications**

551 All images used for cell counting were acquired using a Zeiss LSM 780 confocal or Zeiss
552 Apotome microscope with a 40x objective lens. For each genotype, 3 animals with 1-3 sections
553 of comparable positions per animal were quantified. Areas of interest were outlined and isolated
554 in ImageJ. Nucleus segmentation was carried out using the machine-learning–based
555 segmentation method StarDist (https://github.com/stardist/stardist), which was first trained using
556 manually annotated datasets. Fluorescent label intensity of each channel over nuclear ROIs

557 was calculated by a custom multi-channel intensity quantification algorithm created in OMERO
558 (https://www.openmicroscopy.org/omero/scientists/). Thresholds for signal positivity were
559 manually determined by inspecting each image. Mitosis location, MAFB-labeled cells and OLCs
560 were counted manually in OMERO. For TUJ1 analysis, areas of interest were outlined and the
561 percentage of $TUJ1^+$ regions were measured using the Olympus CellSens Dimension analysis
562 program (Olympus). Image area and ventricular length were measured with Zeiss Zen 3.9
563 imaging software. Data points in all quantification graphs correspond to individual animals,
564 which are the average of 1-3 sections per animal.
565

566 **Western blot**

567 Mouse brains were dissected and total cell lysates were prepared in 20 mM HEPES (pH 7.4),
568 150 mM NaCl, 2% SDS and 5% glycerol supplemented with AEBSF and Halt protease and
569 phosphatase inhibitors (Thermo Fisher Scientific). Protein concentrations were measured by
570 BCA assay (Thermo Scientific). Twenty µg of protein per lane were subjected to SDS-PAGE
571 and probed with primary antibodies and HRP-conjugated secondary antibodies. The following
572 primary antibodies were used: β-actin (Ambion #AM4302, 1:40,000), GAPDH (CST #2118S,
573 1:3000), FLAG (CST #2368S, 1:1000), INSM1 (Santa Cruz sc-271408, 1:500), TEAD1 (CST
574 #12292, 1:500), pan-TEAD (CST #13295, 1:500), and VGLL4 (Thermo Fisher #PA5-58303,
575 1:50). Each lane in Western blot images corresponds to an individual embryo (biological
576 replicate).
577

578 **Co-immunoprecipitation**

579 Plasmids encoding FLAG-tagged proteins were transfected into HEK293T cells plated on 10-cm
580 plates using Lipofectamin 2000. Co-immunoprecipitation was performed 48 h later using
581 Nuclear Complex Co-IP kit (Active Motif #54001) according to kit instruction, using IP Low buffer
582 supplemented with additional detergent to 1% final concentration and 10 µl of Pan-TEAD (CST
583 #13295, 33 µg/ml) or 5 µl of FLAG-M2 (Sigma #F1804, 1 µg/µl) antibody.
584

585 **Proximity ligation assay**

586 The assay was performed according to Duolink kit (Millipore Sigma DUO92103) protocol. The
587 following primary antibodies were used: TEAD1(CST #12292, 1:250), YAP (Sigma
588 WH0010413M1, 1:1000), INSM1 (Santa Cruz Biotechnologies sc-271408 X, 1:50), Ki67 (BD
589 Pharmigen #558615, 1:250) and Ki67 (Vector VP-RM0, 1:250). The images used for the

590 quantification of PLA signals were acquired using a Zeiss LSM 780 confocal microscope and a
591 40x objective lens. The number of spots per image were quantified using OMERO. Each
592 interaction was quantified in 3 embryos. At least 4 images from subpallial sections of
593 comparable positions were quantified for each embryo.
594

595 **Single cell RNA sequencing**

596 MGEs were obtained by first extracting the embryonic brain and detaching the telencephalon,
597 followed by removing the dorsal telencephalon and finally dissecting the MGE from the rest of
598 the subpallium in cold PBS. Both MGEs from the same embryo were dissociated using either
599 Stem-Pro Accutase (Thermo Scientific A1110501) or a papain dissociation kit (Worthington
600 LK003150) for less than 5 min. Cells were filtered through Flowmi cell strainers (SP Bel-Art
601 #13680040). Cell viability was analyzed with a Countess cell counter and only samples with a
602 viability of >90% were processed for scRNAseq. A 3' scRNAseq kit from 10x Genomics was
603 used according to kit instructions. Up to 10K cells were loaded per each bead mix.
604

605 **Single cell RNA sequencing data analysis**

606 General quality control and filtering: Sequences from each individual Illumina sequencing
607 dataset were demultiplexed using bcl2fastq v2.20.0.422 (Illumina). Sequencing reads were
608 processed using 10X Genomics Cell Ranger version 7.0.0, with reads mapping to the mouse
609 reference genome mm10 version 2020-A (10x Genomics). Quality control filtering, clustering,
610 dimensionality reduction, visualization, and differential gene expression were performed using
611 Seurat v4.0.4 with R v4.1.0[38]. Each dataset was initially filtered so that genes that were
612 expressed in at least three or more cells and cells that expressed at least 200 genes were
613 retained when reading in the data. Then cells were excluded if they: (1) expressed greater than
614 10% of unique transcripts derived from mitochondrial genes, (2) unique transcripts derived from
615 mitochondrial genes expressing more than 3 median absolute deviations (MADs) from the
616 median number of unique transcripts derived from mitochondrial genes, (3) had fewer than
617 1,500 genes expressed, or (3) had UMI counts below 5,000. Afterward, cells with more than 3
618 MADs from the median number of genes expressed were removed.
619 Dataset integration processing: Datasets were individually log-normalized using the
620 *NormalizeData* function with default parameters. We calculated 3,000 features that exhibit high
621 cell-to-cell variation in the dataset using the *FindVariableFeature* function. Next, we scaled the
622 data by linear regression against the number of reads using the *ScaleData* function with default
623 parameters. The variable genes were projected onto a low-dimensional subspace using

principal component analysis using the *RunPCA* function with default parameters. The number of principal components (Npcs) were selected based on inspection of the plot of variance explained (Npcs = 30). Datasets were integrated using Harmony integration with default parameters. A shared-nearest-neighbor graph was constructed based on the Euclidean distance in the low-dimensional subspace using the *FindNeighbors* function with dims = 1:30 and default parameters. Integrated datasets then underwent non-linear dimensional reduction and visualization using UMAP. Clusters were identified using a resolution of 0.3. Gene signature scores were calculated using the *AddModuleScore* function with our lists of progenitor genes and neuron genes (Supplementary data 1). Cell cycle phase was inferred using the S- and G2M-phase gene lists from Tirosh, et al 2015 using the *CellCycleScoring* command in Seurat.

Progenitor cluster integration processing: Clusters with average progenitors scores above zero (WT dataset clusters 2,3,6, WT/KO dataset clusters 2,3,5) were subset out and re-analyzed following the above processing steps except that (1) cells with fewer than 2,500 genes expressed were removed and that (2) a list of 742 transcription factor genes (Supplementary data 1) was used as the features to project onto a low-dimensional subspace using principal component analysis using the *RunPCA* function with default parameters. Gene signature scores were calculated using the *AddModuleScore* function with our lists of VZ genes and SVZ-MZ genes (Supplementary data 1). Cell cycle phase was inferred as described above. Pseudotime analysis was conducted using Monocle3 (v1.3.1) with default parameters. Trajectory starting points were manually selected based on the maximum expression of VZ markers. Cluster tree was generated by stepwise (0.025) increasing clustering resolution using progenitor cells from the WT dataset (WT dataset clusters 2,3,6), which identified 0.25 as the optimal resolution. To assign progenitor state annotation to mutant cells, we used the *FindIntegrationAnchors* function in Seurat to detect integration anchors, using the first 30 PCA dimensions between the WT_progenitors_dataset (reference) and the All_progenitors_dataset (query). These anchors were then used to transfer progenitor state labels from the WT_progenitors_dataset to the All_progenitors_dataset. The transfer efficiency was validated by examining the clustering consistency of shared cells between the two datasets, achieving ~93% agreement. The *propeller* function from the speckle_v_0.0.3 package[39] was used to evaluate statistical differences in cell proportions between control and mutants. Pseudotime density plot was generated using the *geom_density* function in ggplot. Differential expression analysis was performed using the *getDE* function in scMINER[42] (https://jyyulab.github.io/scMINER). Gene set enrichment analysis (GSEA) was performed using the *funcEnrich.Fisher* function and visualized

657 with the *draw.funcEnrich.cluster* function in NetBID2[43] (https://jyyulab.github.io/NetBID).
658 Selected gene sets were visualized with the *draw.GSEA* function in NetBID2.
659

660 **Calculation of in vivo cell cycle parameters**

661 Pregnant dams were injected intraperitoneally with EdU (10 µg/g body weight) and followed by
662 BrdU (50 µg/g body weight) 1.5 h later. Dams were euthanized 30-min following BrdU
663 administration, and embryos were collected and processed for cryosectioning. Sections were
664 blocked in PBS containing 3% normal donkey serum and 0.2% Triton X-100, incubated in
665 primary antibodies against ASCL1 and OLIG2 at 4°C overnight, washed in PBS, and incubated
666 in fluorescence-conjugated secondary antibodies for 2 h at room temperature. After 3 washes
667 in PBS, sections were post-fixed in 4% paraformaldehyde for 10 min, followed by 3 washes in
668 PBS. To detect EdU, sections were incubated in 1N HCl at 45°C for 30 min, then washed 3
669 times in PBS. EdU was detected by the Click-it Plus EdU Alexa Fluor 488 Imaging Kit (Thermo
670 Scientific Invitrogen #C10337). Sections were then washed 3 times in PBS, blocked again in
671 PBS containing 3% normal donkey serum and 0.2% Triton X-100, incubated in BrdU antibody
672 (Abcam #ab6326, 1:100) overnight at 4°C and secondary antibody for 2 h at room temperature.
673 After 3 washes in PBS, sections were coverslipped in ProLong Gold. Z-stack images (5) were
674 acquired on a Zeiss LSM 780 confocal microscope, merged in ImageJ, and quantified with
675 OMERO.
676 Cell cycle parameters were calculated based on the method described by Quinn et al[40].
677 The following populations were quantified using OMERO: Cycling fraction ($Cycling_{fraction}$): total
678 number of cells in each progenitor subtype defined as $OLIG2^{+}ASCL1^{-}$, $OLIG2^{+}ASCL1^{+}$, and
679 $OLIG2^{-}ASCL1^{+}$; S-phase fraction ($S_{fraction}$): the number of progenitor cells in the S phase,
680 defined as $EdU^{+}BrdU^{+}$ cells; Leaving fraction ($L_{fraction}$): the number of progenitor cells that have
681 left the S phase, defined as $EdU^{+}BrdU^{-}$ cells. S-phase length (T_S) and total cell-cycle length
682 (T_C) were then calculated using the following equations: (1) $\frac{T_S}{T_L} = \frac{S_{fraction}}{L_{fraction}}$; (2) $T_s = \frac{S_{fraction}}{L_{fraction}} \times T_L$;
683 (3) $T_s = \frac{S_{fraction}}{L_{fraction}} \times 1.5$; (4) $\frac{T_C}{T_S} = \frac{Cycling_{fraction}}{S_{fraction}}$; (5) $T_C = \frac{Cycling_{fraction}}{S_{fraction}} \times T_S$.
684

685 **FlashTag labeling of neural progenitor cells in vivo**

686 The procedure was performed according to the protocol described by Govindan et al[41].
687 Pregnant mice carrying E12.5 embryos were deeply anesthetized with 2.5–3% of isoflurane and
688 the uterine horns exposed. Approximately 300 nL of 10 mM carboxyfluorescein succinimidyl

689 ester (CFSE, Invitrogen C34554) in DMSO was injected into a lateral ventricle of the embryo
690 brain using a pulled glass micropipette. Embryos were returned to dam and allowed to
691 resume normal development before being harvested for immunostaining.
692

693 **RNAscope in situ hybridization**

694 Tissue sections were processed according to the kit instructions for frozen samples (Advanced
695 Cell Diagnostics (ACD) RNAscope Multiplex FL v2 #323100). Sections were air-dried for 1 h at
696 room temperature and further dried at 60°C for 30 min. Slides were post-fixed in 4%
697 paraformaldehyde for 15 min at 4°C, followed by dehydration in graded ethanol (50%, 70%, and
698 100% ethanol) for 5 min each, with a final dehydration step in 100% ethanol for 5 min. Sections
699 were then air-dried for 5 min at 60°C. Endogenous peroxidase activity was quenched in H_2O_2 for
700 10 min, followed by 3 washes with distilled water (dH_2O). Sections were further dehydrated in
701 100% ethanol for 3 min and dried for 5 min at 60°C. Tissue was permeabilized with Protease III
702 for 20 min at 40°C. Slides were then washed twice in dH_2O for 2 min. Sections were incubated
703 with a probe mixture targeting MmHes5 (ACD #400991, C2) and MmNotch1 (ACD #404641,
704 C4), each at a 1:100 dilution in probe diluent (ACD #300041) for 2 h at 40°C. Signal
705 amplification was carried out using the RNAscope amplification reagents (AMP1, AMP2, and
706 AMP3), with incubation at 40°C for 30 min each for AMP1/2 and 15 min for AMP3. After each
707 amplification step, sections were washed twice for 2 min with ACD wash buffer. HRP signal was
708 developed for 15 min at 40°C, followed by washing and incubation with the appropriate
709 fluorophores: Opal 520 (for C2 at 1:1000) (FP1487001KT) and Opal 570 (for C4 at 1:1000)
710 (FP1488001KT) for 30 min at 40°C. After a final round of washing, sections were blocked with
711 RNAscope HRP blocker for 15 min at 40°C. Nuclei were stained with DAPI. Slides were then
712 mounted in Prolong Gold. Fluorescent images were acquired using a Zeiss Apotome
713 microscope. Laser power and exposure time was adjusted to ensure below saturation exposure.
714 Quantification was performed in ImageJ. The mean fluorescence intensity (total fluorescence
715 signal divided by area) of *Hes5* and *Notch1* was measured in the medial ganglionic eminence
716 (MGE) and a cortical VZ region within the same section. Because the cortex of *Tead1;2* dKO
717 mice did not shown obvious morphological phenotype, the cortex was used as an internal
718 control. The average mean intensity values from the left and right MGE were normalized to the
719 mean intensity values in the cortex.
720

721 **Statistical analysis**

722 Statistical analyses of immunostaining and RNAscope experiments were done using GraphPad
723 Prism software. Statistical significance was assessed by unpaired two-tailed t-test. $P < 0.05$ was
724 considered a significant difference. Individual animals are defined as a biological replicated. All
725 values represent individual animals mean ± SEM (standard error of the mean). The statistical
726 test used and the P values are indicated in figures or figure legends. Statistical analyses of
727 scRNA-seq data were performed using designated functions in *propeller* (cell proportions),
728 scMINER (differential gene expression), and NetBID2 (gene set enrichment analysis).
729

730 ## Data availability

731 The raw single-cell RNA sequencing datasets generated in this study have been deposited in
732 the GEO repository databased under the accession code GSE.
733

734 ## Material availability

735 Correspondence and requests for materials should be addressed to X.C.
736

737 ## Code availability

738 The code for the scRNA-seq analysis presented in this manuscript in available on
739 https://github.com/thecaolab-stjude/subpallium_development_Tead_and_YT_KO
740

741 ## References

742 1 Moreno, N., González, A. & Rétaux, S. Development and evolution of the subpallium.
743 *Semin Cell Dev Biol* **20**, 735-743 (2009). https://doi.org/10.1016/j.semcdb.2009.04.007
744 2 Turrero Garcia, M. & Harwell, C. C. Radial glia in the ventral telencephalon. *FEBS letters*
745 **591**, 3942-3959 (2017). https://doi.org/10.1002/1873-3468.12829
746 3 Anderson, S. A., Eisenstat, D. D., Shi, L. & Rubenstein, J. L. Interneuron migration from
747 basal forebrain to neocortex: dependence on Dlx genes. *Science* **278**, 474-476 (1997).
748 https://doi.org/10.1126/science.278.5337.474
749 4 Kessaris, N. *et al.* Competing waves of oligodendrocytes in the forebrain and postnatal
750 elimination of an embryonic lineage. *Nature Neuroscience* **9**, 173-179 (2006).
751 https://doi.org/10.1038/nn1620
752 5 Taverna, E., Götz, M. & Huttner, W. B. The cell biology of neurogenesis: toward an
753 understanding of the development and evolution of the neocortex. *Annu Rev Cell Dev Biol*
754 **30**, 465-502 (2014). https://doi.org/10.1146/annurev-cellbio-101011-155801
755 6 Kriegstein, A. & Alvarez-Buylla, A. The glial nature of embryonic and adult neural stem
756 cells. *Annu Rev Neurosci* **32**, 149-184 (2009).
757 https://doi.org/10.1146/annurev.neuro.051508.135600
758 7 Smart, I. H. A pilot study of cell production by the ganglionic eminences of the developing
759 mouse brain. *Journal of anatomy* **121**, 71-84 (1976).

8 Fentress, J. C., Stanfield, B. B. & Cowan, W. M. Observation on the development of the striatum in mice and rats. *Anatomy and embryology* **163**, 275-298 (1981). https://doi.org/10.1007/bf00315705

9 Pilz, G.-A. *et al.* Amplification of progenitors in the mammalian telencephalon includes a new radial glial cell type. *Nature Communications* **4**, 2125 (2013). https://doi.org/10.1038/ncomms3125

10 Zheng, Y. & Pan, D. The Hippo Signaling Pathway in Development and Disease. *Developmental Cell* **50**, 264-282 (2019). https://doi.org/10.1016/j.devcel.2019.06.003

11 Driskill, J. H. & Pan, D. Control of stem cell renewal and fate by YAP and TAZ. *Nat Rev Mol Cell Biol* **24**, 895-911 (2023). https://doi.org/10.1038/s41580-023-00644-5

12 Zhong, Z., Jiao, Z. & Yu, F.-X. The Hippo signaling pathway in development and regeneration. *Cell Reports* **43** (2024). https://doi.org/10.1016/j.celrep.2024.113926

13 Lavado, A. *et al.* YAP/TAZ maintain the proliferative capacity and structural organization of radial glial cells during brain development. *Dev Biol* **480**, 39-49 (2021). https://doi.org/10.1016/j.ydbio.2021.08.010

14 Lin, K. C., Park, H. W. & Guan, K. L. Regulation of the Hippo Pathway Transcription Factor TEAD. *Trends in biochemical sciences* **42**, 862-872 (2017). https://doi.org/10.1016/j.tibs.2017.09.003

15 Landin-Malt, A., Benhaddou, A., Zider, A. & Flagiello, D. An evolutionary, structural and functional overview of the mammalian TEAD1 and TEAD2 transcription factors. *Gene* **591**, 292-303 (2016). https://doi.org/https://doi.org/10.1016/j.gene.2016.07.028

16 Sebé-Pedrós, A., Zheng, Y., Ruiz-Trillo, I. & Pan, D. Premetazoan Origin of the Hippo Signaling Pathway. *Cell Reports* **1**, 13-20 (2012). https://doi.org/https://doi.org/10.1016/j.celrep.2011.11.004

17 Phillips, J. E., Zheng, Y. & Pan, D. Assembling a Hippo: the evolutionary emergence of an animal developmental signaling pathway. *Trends in biochemical sciences* **49**, 681-692 (2024). https://doi.org/https://doi.org/10.1016/j.tibs.2024.04.005

18 Grunberg, H. Ein beitrag zur kenntnis der roentgen-mutationen des X-chromosomes von Drosophila melanogaster. *Biol. Zent.* **17476**, 680-694 (1929).

19 Halder, G. *et al.* The Vestigial and Scalloped proteins act together to directly regulate wing-specific gene expression in Drosophila. *Genes & Development* **12**, 3900-3909 (1998). https://doi.org/10.1101/gad.12.24.3900

20 Simmonds, A. J. *et al.* Molecular interactions between Vestigial and Scalloped promote wing formation in Drosophila. *Genes & Development* **12**, 3815-3820 (1998). https://doi.org/10.1101/gad.12.24.3815

21 Wu, J., Duggan, A. & Chalfie, M. Inhibition of touch cell fate by egl-44 and egl-46 in C. elegans. *Genes & Development* **15**, 789-802 (2001). https://doi.org/10.1101/gad.857401

22 Feng, G. *et al.* Developmental stage-dependent transcriptional regulatory pathways control neuroblast lineage progression. *Development* **140**, 3838 (2013). https://doi.org/10.1242/dev.098723

23 Iwasa, H. *et al.* Yes-associated protein homolog, YAP-1, is involved in the thermotolerance and aging in the nematode Caenorhabditis elegans. *Experimental Cell Research* **319**, 931-945 (2013). https://doi.org/https://doi.org/10.1016/j.yexcr.2013.01.020

24 Cao, X., Pfaff, S. L. & Gage, F. H. YAP regulates neural progenitor cell number via the TEA domain transcription factor. *Genes Dev* **22**, 3320-3334 (2008). https://doi.org/10.1101/gad.1726608

25 Englund, C. *et al.* Pax6, Tbr2, and Tbr1 are expressed sequentially by radial glia, intermediate progenitor cells, and postmitotic neurons in developing neocortex. *The Journal of neuroscience : the official journal of the Society for Neuroscience* **25**, 247-251 (2005). https://doi.org/10.1523/jneurosci.2899-04.2005

26 Yun, K. *et al.* Modulation of the notch signalling by Mash1 and Dlx1/2 regulates sequential specification and differentiation of progenitor cell types in the subcortical telencephalon. *Development* **129**, 5029-5040 (2002).
27 Petryniak, M. A., Potter, G. B., Rowitch, D. H. & Rubenstein, J. L. R. Dlx1 and Dlx2 Control Neuronal versus Oligodendroglial Cell Fate Acquisition in the Developing Forebrain. *Neuron* **55**, 417-433 (2007). https://doi.org/https://doi.org/10.1016/j.neuron.2007.06.036
28 Imayoshi, I. *et al.* Oscillatory control of factors determining multipotency and fate in mouse neural progenitors. *Science* **342**, 1203-1208 (2013). https://doi.org/10.1126/science.1242366
29 Milewski, R. C. *et al.* Identification of minimal enhancer elements sufficient for Pax3 expression in neural crest and implication of Tead2 as a regulator of Pax3. *Development* **131**, 829 (2004). https://doi.org/10.1242/dev.00975
30 Imayoshi, I. *et al.* Oscillatory Control of Factors Determining Multipotency and Fate in Mouse Neural Progenitors. *Science* **342**, 1203-1208 (2013). https://doi.org/doi:10.1126/science.1242366
31 Rubenstein, J. L. R. & Campbell, K. in *Patterning and Cell Type Specification in the Developing CNS and PNS* (eds John L. R. Rubenstein & Pasko Rakic) Ch. 24 - Neurogenesis in the Basal Ganglia, 455-473 (Academic Press, 2013).
32 Mayer, C. *et al.* Developmental diversification of cortical inhibitory interneurons. *Nature* **555**, 457 (2018). https://doi.org/10.1038/nature25999 https://www.nature.com/articles/nature25999#supplementary-information
33 Pai, E. L.-L. *et al.* Mafb and c-Maf Have Prenatal Compensatory and Postnatal Antagonistic Roles in Cortical Interneuron Fate and Function. *Cell Reports* **26**, 1157-1173.e1155 (2019). https://doi.org/https://doi.org/10.1016/j.celrep.2019.01.031
34 Rowitch, D. H. Glial specification in the vertebrate neural tube. *Nature Reviews Neuroscience* **5**, 409-419 (2004). https://doi.org/10.1038/nrn1389
35 Mi, D. *et al.* Early emergence of cortical interneuron diversity in the mouse embryo. *Science* **360**, 81-85 (2018). https://doi.org/10.1126/science.aar6821
36 Su-Feher, L. *et al.* Single cell enhancer activity distinguishes GABAergic and cholinergic lineages in embryonic mouse basal ganglia. *Proc Natl Acad Sci U S A* **119**, e2108760119 (2022). https://doi.org/10.1073/pnas.2108760119
37 *Allen Institute for Brain Science. Allen Brain Atlas Developing Mouse Brain [dataset]*, <http://developingmouse.brain-map.org/> (
38 Stuart, T. *et al.* Comprehensive Integration of Single-Cell Data. *Cell* **177**, 1888-1902.e1821 (2019). https://doi.org/10.1016/j.cell.2019.05.031
39 Phipson, B. *et al.* propeller: testing for differences in cell type proportions in single cell data. *Bioinformatics* **38**, 4720-4726 (2022). https://doi.org/10.1093/bioinformatics/btac582
40 Quinn, J. C. *et al.* Pax6 controls cerebral cortical cell number by regulating exit from the cell cycle and specifies cortical cell identity by a cell autonomous mechanism. *Developmental Biology* **302**, 50-65 (2007). https://doi.org/https://doi.org/10.1016/j.ydbio.2006.08.035
41 Govindan, S., Oberst, P. & Jabaudon, D. In vivo pulse labeling of isochronic cohorts of cells in the central nervous system using FlashTag. *Nature Protocols* **13**, 2297-2311 (2018). https://doi.org/10.1038/s41596-018-0038-1
42 Ding, L. *et al.* scMINER: a mutual information-based framework for identifying hidden drivers from single-cell omics data. *bioRxiv* (2023). https://doi.org/10.1101/2023.01.26.523391
43 Dong, X. *et al.* NetBID2 provides comprehensive hidden driver analysis. *Nat Commun* **14**, 2581 (2023). https://doi.org/10.1038/s41467-023-38335-6

44 Mason, H. A. *et al.* Notch signaling coordinates the patterning of striatal compartments. *Development* **132**, 4247-4258 (2005). https://doi.org/10.1242/dev.02008

45 Koontz, Laura M. *et al.* The Hippo Effector Yorkie Controls Normal Tissue Growth by Antagonizing Scalloped-Mediated Default Repression. *Developmental Cell* **25**, 388-401 (2013). https://doi.org/https://doi.org/10.1016/j.devcel.2013.04.021

46 Guo, T. *et al.* A novel partner of Scalloped regulates Hippo signaling via antagonizing Scalloped-Yorkie activity. *Cell Research* **23**, 1201 (2013). https://doi.org/https://doi.org/10.1038/cr.2013.120

47 Vissers, J. H. A. *et al.* The Scalloped and Nerfin-1 Transcription Factors Cooperate to Maintain Neuronal Cell Fate. *Cell Rep* **25**, 1561-1576.e1567 (2018). https://doi.org/10.1016/j.celrep.2018.10.038

48 Guo, P. *et al.* Nerfin-1 represses transcriptional output of Hippo signaling in cell competition. *eLife* **8** (2019). https://doi.org/10.7554/eLife.38843

49 Qiao, Y. *et al.* RUNX3 is a novel negative regulator of oncogenic TEAD-YAP complex in gastric cancer. *Oncogene* **35**, 2664-2674 (2016). https://doi.org/10.1038/onc.2015.338

50 Suo, J. *et al.* VGLL4 promotes osteoblast differentiation by antagonizing TEADs-inhibited Runx2 transcription. *Sci Adv* **6** (2020). https://doi.org/10.1126/sciadv.aba4147

51 Lin, Z. *et al.* Acetylation of VGLL4 Regulates Hippo-YAP Signaling and Postnatal Cardiac Growth. *Dev Cell* **39**, 466-479 (2016). https://doi.org/10.1016/j.devcel.2016.09.005

52 Cai, J. *et al.* YAP-VGLL4 antagonism defines the major physiological function of the Hippo signaling effector YAP. *Genes Dev* **36**, 1119-1128 (2022). https://doi.org/10.1101/gad.350127.122

53 Yu, W. *et al.* VGLL4 plays a critical role in heart valve development and homeostasis. *PLoS Genet* **15**, e1007977 (2019). https://doi.org/10.1371/journal.pgen.1007977

54 Welcker, J. E. *et al.* Insm1 controls development of pituitary endocrine cells and requires a SNAG domain for function and for recruitment of histone-modifying factors. *Development* **140**, 4947 (2013). https://doi.org/10.1242/dev.097642

55 Duggan, A. *et al.* Transient expression of the conserved zinc finger gene INSM1 in progenitors and nascent neurons throughout embryonic and adult neurogenesis. *Journal of Comparative Neurology* **507**, 1497-1520 (2008). https://doi.org/10.1002/cne.21629

56 Farkas, L. M. *et al.* Insulinoma-associated 1 has a panneurogenic role and promotes the generation and expansion of basal progenitors in the developing mouse neocortex. *Neuron* **60**, 40-55 (2008). https://doi.org/10.1016/j.neuron.2008.09.020

57 Tavano, S. *et al.* Insm1 Induces Neural Progenitor Delamination in Developing Neocortex via Downregulation of the Adherens Junction Belt-Specific Protein Plekha7. *Neuron* **97**, 1299-1314.e1298 (2018). https://doi.org/https://doi.org/10.1016/j.neuron.2018.01.052

58 Monaghan, C. E. *et al.* REST corepressors RCOR1 and RCOR2 and the repressor INSM1 regulate the proliferation–differentiation balance in the developing brain. *Proceedings of the National Academy of Sciences* **114**, E406 (2017). https://doi.org/10.1073/pnas.1620230114

59 Allaway, K. C. *et al.* Genetic and epigenetic coordination of cortical interneuron development. *Nature* **597**, 693-697 (2021). https://doi.org/10.1038/s41586-021-03933-1

60 Jacob, J. *et al.* Insm1 (IA-1) is an essential component of the regulatory network that specifies monoaminergic neuronal phenotypes in the vertebrate hindbrain. *Development* **136**, 2477-2485 (2009). https://doi.org/10.1242/dev.034546

61 Wiwatpanit, T. *et al.* Trans-differentiation of outer hair cells into inner hair cells in the absence of INSM1. *Nature* **563**, 691-695 (2018). https://doi.org/10.1038/s41586-018-0570-8

62 Tronche, F. *et al.* Disruption of the glucocorticoid receptor gene in the nervous system results in reduced anxiety. *Nat Genet* **23**, 99-103 (1999). https://doi.org/10.1038/12703

63 Yang, X. *et al.* Notch activation induces apoptosis in neural progenitor cells through a p53-dependent pathway. *Dev Biol* **269**, 81-94 (2004). https://doi.org/10.1016/j.ydbio.2004.01.014

64 Kaneko, K. J., Kohn, M. J., Liu, C. & DePamphilis, M. L. Transcription factor TEAD2 is involved in neural tube closure. *Genesis* **45**, 577-587 (2007). https://doi.org/10.1002/dvg.20330

65 Xin, M. *et al.* Regulation of insulin-like growth factor signaling by Yap governs cardiomyocyte proliferation and embryonic heart size. *Sci Signal* **4**, ra70 (2011).

Acknowledgements

We thank members of the Cao lab for suggestions and technical help; Aaron Taylor and George Campbell for help in image acquisition; Abbas Shirinifard for help in image quantification; Yiping Fan and Hongjian Jin for help in scRNA-seq data analysis; Shondra Miller, Valerie Stewart, and members of the Center for Advanced Genomic Editing and of the Neuroembryology core at St. Jude Children's Research Hospital (SJCRH) for generating the *Vgll4*^{F} alleles; Melvin DePamphilis, Eric Olson, and Jaime García-Añoveros for sharing mouse lines. This work was supported by National Institute of Health grant R01NS119760 (to X.C. and J.Y.), P30CA021765 (to SJCRH Comprehensive Cancer Center core facilities), and American Lebanese Syrian Associated Charities (ALSAC).

Author contributions

X.C. conceived and supervised the project; C.P and A.L. performed the majority of the experiments and data analysis; A.L., V.T., C.R., A.M., J.Y. and J.Y performed computational analysis of scRNA-seq data; J.P. helped with mouse management and Western blotting; R.D. helped with histological analysis. X.C. wrote the paper with input from other authors.

Competing interests

The authors declare no competing interests.

Correspondence and requests for materials should be addressed to Xinwei Cao.

Fig. 1

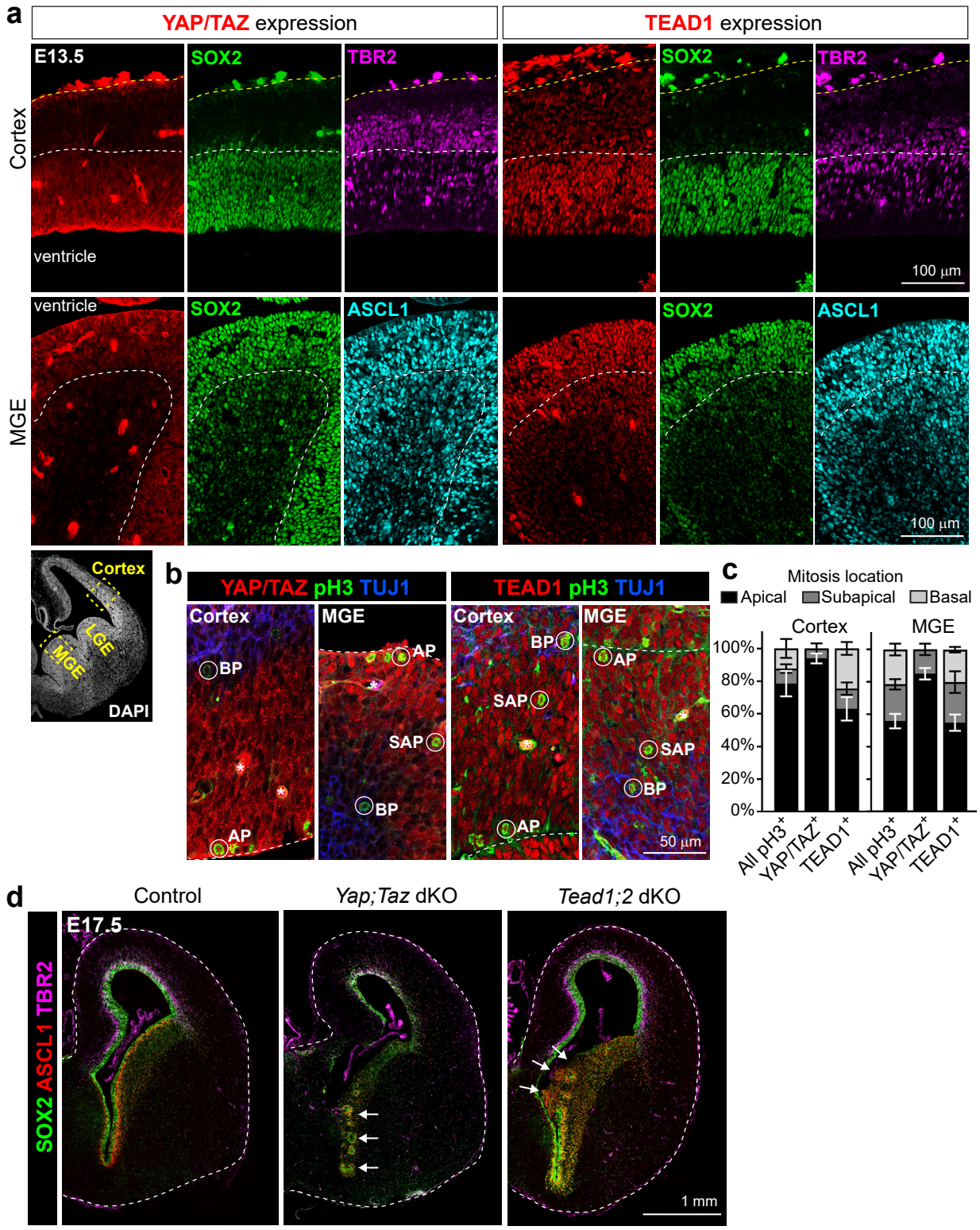
a
YAP/TAZ expression
TEAD1 expression
E13.5
SOX2
TBR2
Cortex
ventricle
100 µm
MGE
ASCL1
Cortex
LGE
MGE
DAPI
b
YAP/TAZ pH3 TUJ1
TEAD1 pH3 TUJ1
Cortex
MGE
BP
AP
SAP
50 µm
c
Mitosis location
Apical
Subapical
Basal
100%
80%
60%
40%
20%
0%
All pH3+
YAP/TAZ+
TEAD1+
d
Control
Yap;Taz dKO
Tead1;2 dKO
E17.5
SOX2 ASCL1 TBR2
1 mm

Fig. 1 | Expression patterns of YAP/TAZ and TEAD in the developing forebrain and gross phenotypes of their mutants. a YAP/TAZ and TEAD1 expression patterns in E13.5 forebrain sections examined by immunostaining. White dashed lines delineate the boundary between the ventricular zone (VZ) and the subventricular zone (SVZ). Yellow dashed lines mark the outer surface of the cortex. MGE, medial ganglionic eminence; LGE, lateral ganglionic eminence. **b** YAP/TAZ and TEAD1 immunostaining on E13.5 forebrain sections co-stained with phospho-histone H3 (pH3, cells in mitosis) and βIII-tubulin (TUJ1, neurons), highlighting apical progenitors (APs) that divide at the ventricular surface (VS), subapical progenitors (SAPs) that divided at subapical positions within the VZ, and basal progenitors (BPs) that divide in the SVZ. Dashed lines delineate the VS. Asterisks, autofluorescent blood vessels. **c** Quantification of the proportion of $pH3^+$ cells at the respective locations. Values are mean ± SEM. **d** Immunostaining showing the gross phenotypes of *Nestin-Cre* mediated *Yap;Taz* double knockout (dKO) and *Tead1;2* dKO forebrain at E17.5. Dashed lines mark the outer surface of the forebrain. Arrows highlight disruptions in the VS and VZ-SVZ organization.

Sup. Fig. 1

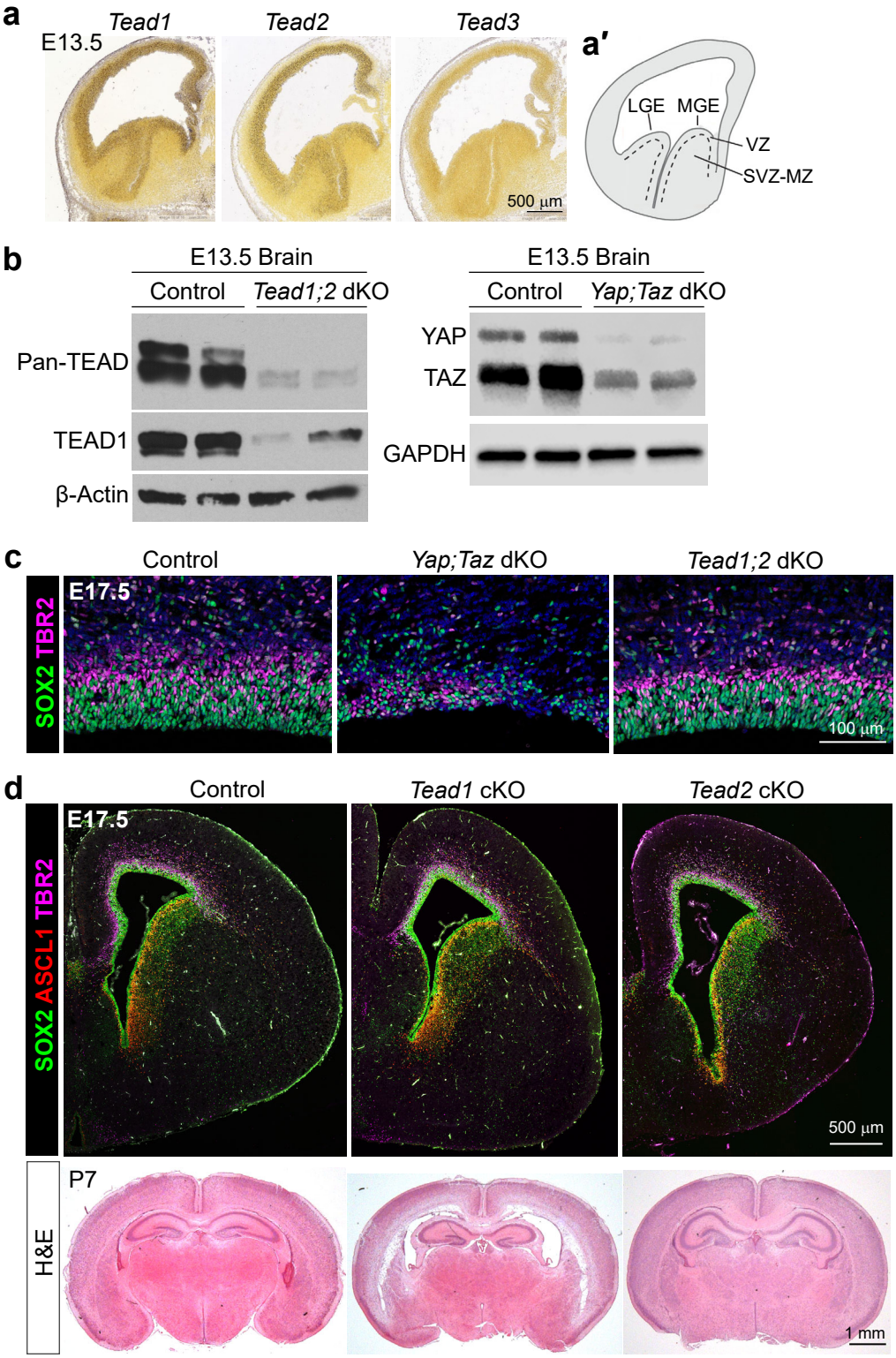
a
E13.5
Tead1
Tead2
Tead3
500 µm
a′
LGE
MGE
VZ
SVZ-MZ
b
E13.5 Brain
Control
Tead1;2 dKO
Pan-TEAD
TEAD1
β-Actin
E13.5 Brain
Control
Yap;Taz dKO
YAP
TAZ
GAPDH
c
Control
Yap;Taz dKO
Tead1;2 dKO
SOX2 TBR2
E17.5
100 µm
d
Control
Tead1 cKO
Tead2 cKO
SOX2 ASCL1 TBR2
E17.5
500 µm
H&E
P7
1 mm

Supplementary Fig. 1 | Expression patterns of *Tead* genes in the developing telencephalon and the gross phenotypes of *Yap;Taz* and *Tead* knockout mice. a RNA in situ hybridization images of *Tead1–3* genes (Allen Developing Mouse Brain Atlas). **a′** A schematic of the E13.5 telencephalon showing subpallial regional organization. LGE, lateral ganglionic eminence; MGE, medial ganglionic eminence; VZ, ventricular zone; SVZ, subventricular zone; MZ, mantle zone. **b** Western blot analysis of total brain lysates from no-*Cre* control and *Nestin-Cre*–mediated *Tead1* and *Tead2* double knockout (*Tead1;2* dKO) and *Yap* and *Taz* (*Yap;Taz*) dKO mice. Note that a TEAD2 specific antibody was not available to us. Nevertheless, a pan-TEAD antibody showed that the levels of TEAD proteins were strongly reduced in *Tead1;2* dKO brains. **c** Immunostaining showing the neocortex of control and dKO mice, focusing on the VZ and SVZ regions. Blue color is DAPI signal. **d** Immunostaining and H&E staining showing the gross brain morphology of *Nestin-Cre*–mediated *Tead1* and *Tead2* single conditional knockout (cKO) mice.

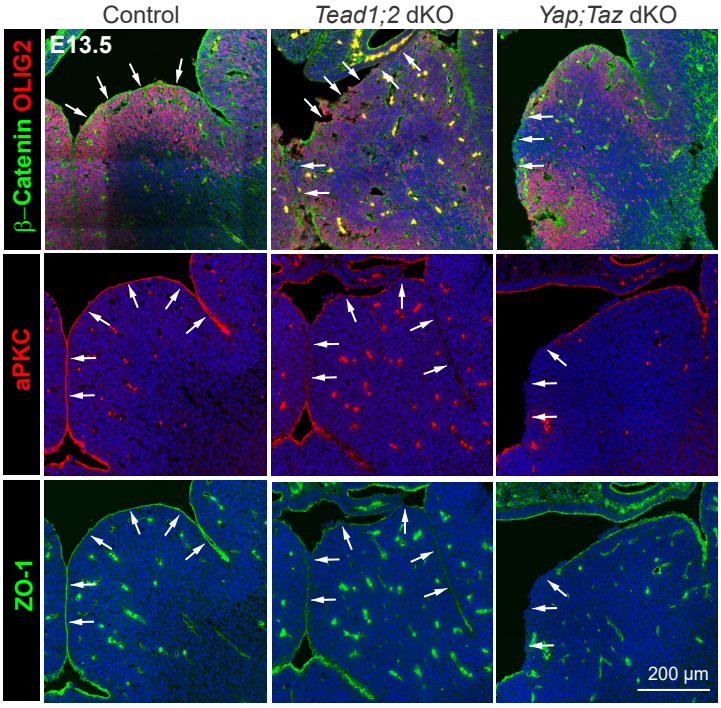

Supplementary Fig. 2 | TEAD1/2 loss and YAP/TAZ loss similarly disrupt subpallial neuroepithelial apical juctions. Immunostaining with apical junction markers β-catenin, aPKC, and ZO-1 showing the medial ganglionic eminence. Arrows: apical junctions. Blue color is DAPI signal.

Fig. 2

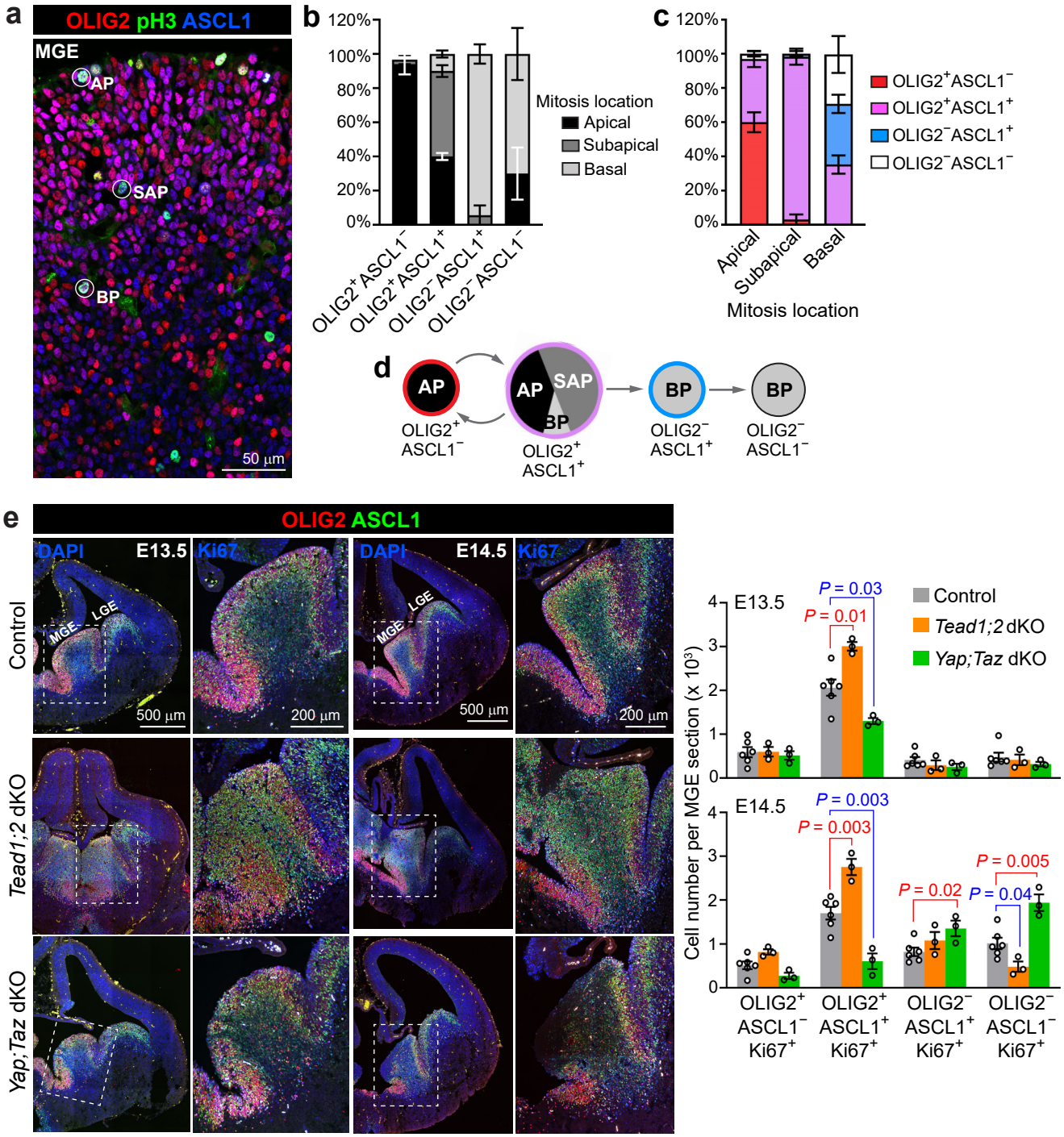

Fig. 2 | TEAD1/2 loss and YAP/TAZ loss have distinct impacts on the lineage progression of subpallial neural progenitors. a Immunostaining on a E13.5 brain section, highlighting an apical progenitor (AP), a subapical progenitor (SAP), and a basal progenitor (BP). **b**, **c** Quantification of the proportion of pH3⁺ cells found at different locations. **d** A schematic of proposed progenitor states during subpallial neural progenitor lineage progression. **e** Immunostaining and quantification of progenitors in each of the states defined by OLIG2 and ASCL1 immunosignal. N = 6 control mice with 3 from each line, N = 3 dKO mice. Areas in dashed boxes are enlarged in the images to the right. MGE, medial ganglionic eminence. LGE, lateral ganglionic eminence. Values in b, c, and e are mean ± SEM. Each data point represents an individual animal. Two-sided unpaired *t*-test. Unmarked comparisons (vs. control) did not show significant difference ($P > 0.05$).

Fig. 3

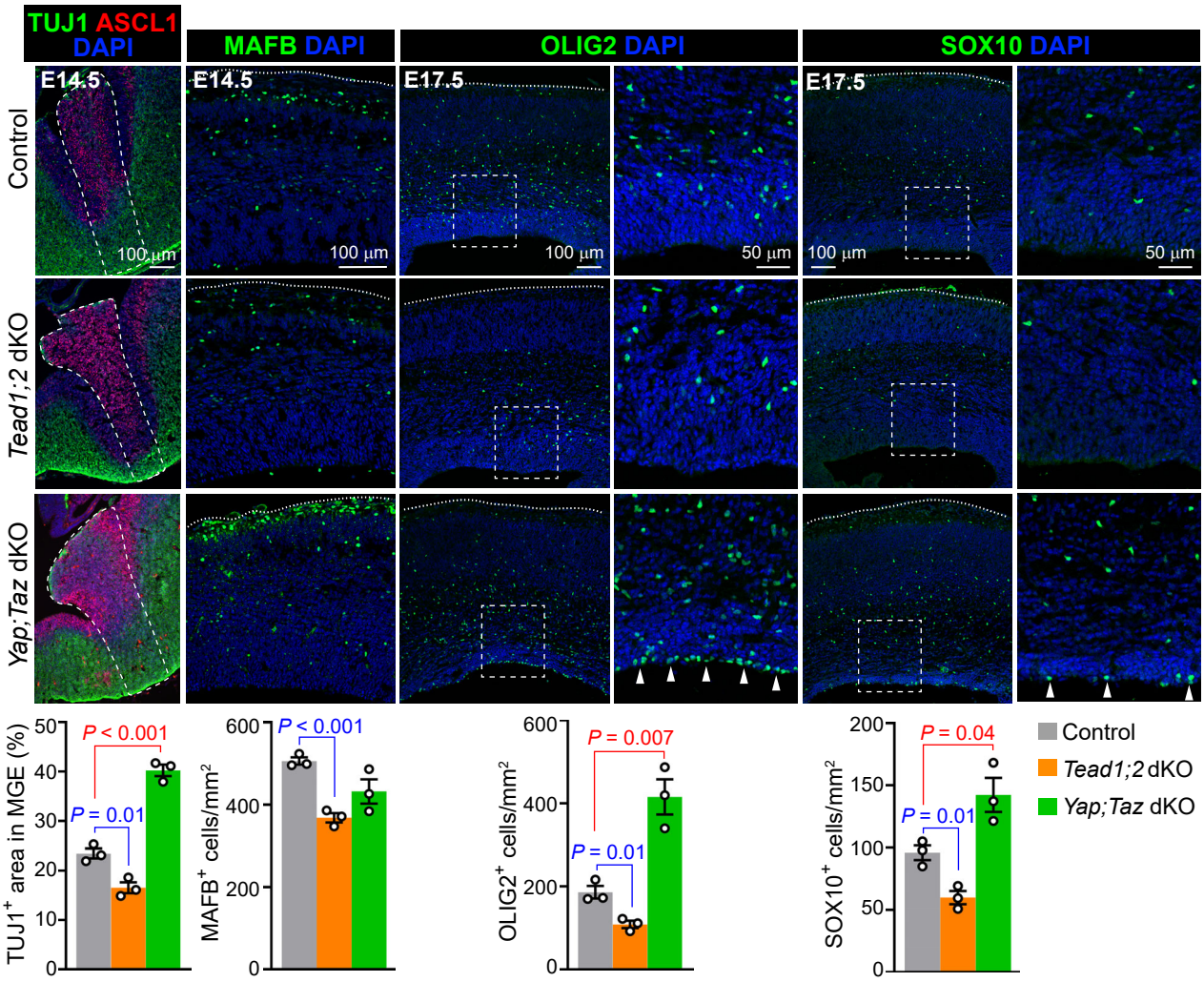

Fig. 3 | TEAD1/2 loss and YAP/TAZ loss have distinct impacts on the cellular output from subpallial progenitors. Immunostaining and quantification of neurons (TUJ1) in the MGE (dashed area), and immature interneurons (MAFB) and oligodendrocyte lineage cells (OLIG2 and SOX10) in the neocortex. Dotted lines mark the outer surface of the cortex. Areas in dashed boxes are enlarged in the images to the right. Values are mean ± SEM. Each data point represents an individual animal. Two-sided unpaired *t*-test. Unmarked comparisons (vs. control) did not show significant difference ($P > 0.05$).

Fig. 4

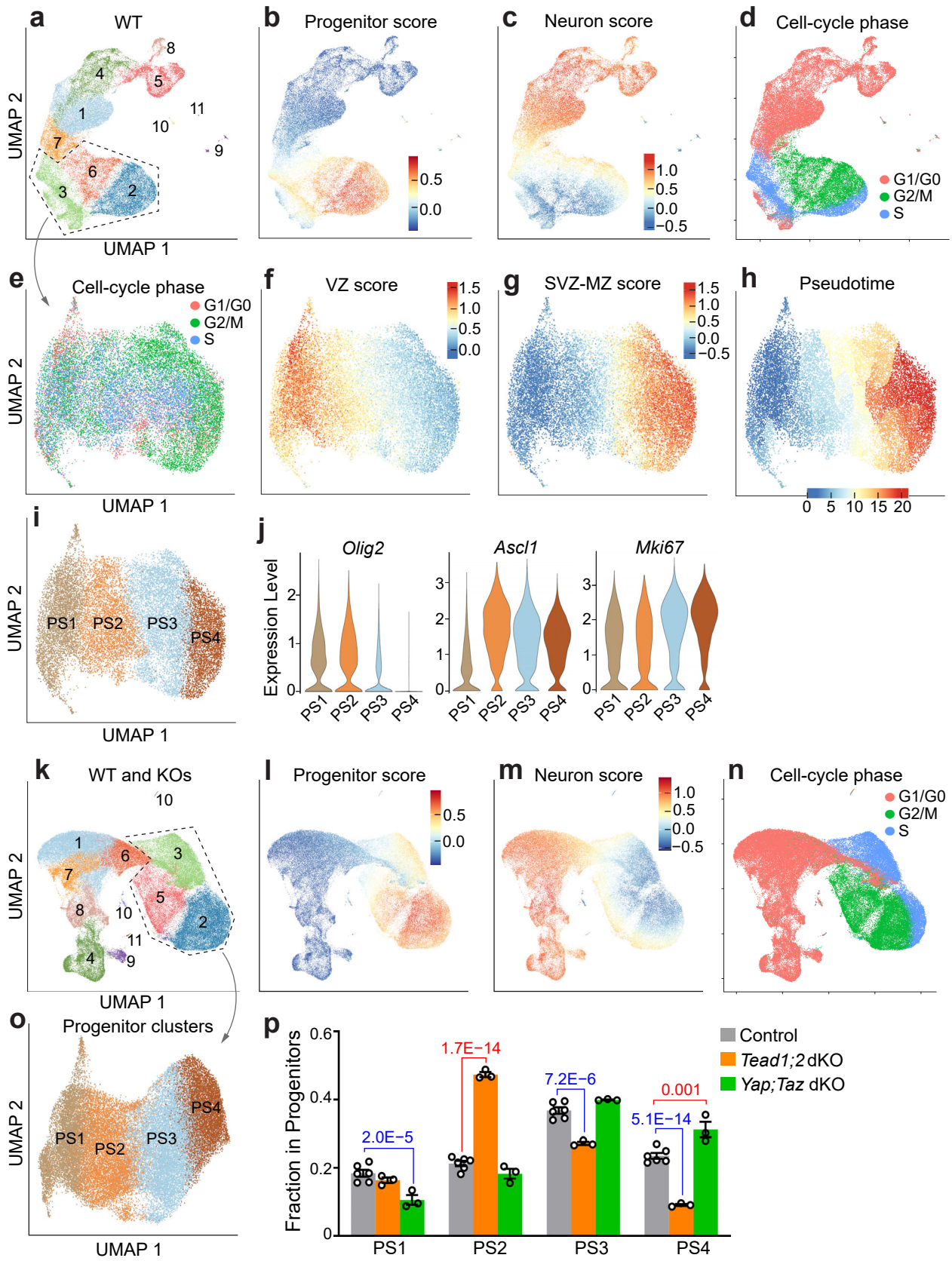
a
WT
UMAP 2
UMAP 1
b
Progenitor score
c
Neuron score
d
Cell-cycle phase
G1/G0
G2/M
S
e
Cell-cycle phase
f
VZ score
g
SVZ-MZ score
h
Pseudotime
i
PS1
PS2
PS3
PS4
j
Olig2
Ascl1
Mki67
Expression Level
k
WT and KOs
l
Progenitor score
m
Neuron score
n
Cell-cycle phase
o
Progenitor clusters
p
Fraction in Progenitors
Control
Tead1;2 dKO
Yap;Taz dKO
2.0E−5
1.7E−14
7.2E−6
5.1E−14
0.001

Fig. 4 | Single-cell RNA sequencing analysis reveals distinct impacts of TEAD1/2 loss and YAP/TAZ loss on MGE neural progenitor lineage progression. a Clustering of WT MGE cells (which included E12.5 WT, E14.5 *Tead1;2* control, and E15.5 WT cells; n = 42,876 cells after quality control) based on highly variable genes (HVG) visualized by UMAP. **b–d** UMAP visualizations of progenitor score, neuron score, and cell-cycle phase of WT MGE cells. **e** Cell cycle phase of WT progenitor cells (cells from clusters 2, 3, and 6 in **a**; n = 18,963 cells after quality control) visualized by UMAP using a curated list of transcription factors for feature selection. **f–h** UMAP visualizations of VZ score, SVZ-MZ score, and pseudotime of WT progenitor cells. **i** Clustering of WT progenitor cells based on the list of transcription factors at the resolution of 0.25. PS, progenitor state. **j** ScRNA-seq expression levels of indicated genes in each progenitor state. **k** Clustering of WT and KO MGE cells (which included E12.5 WT, E14.5 *Tead1;2* control and dKO, E14.5 *Yap;Taz* control and dKO, and E15.5 WT cells; n = 85,684 cells after quality control) based on HVG visualized by UMAP. **l–n** UMAP visualizations of progenitor score, neuron score, and cell-cycle phase of WT and KO cells. **o** Progenitor state annotation of progenitor cells (cells from clusters 2, 3, and 5 in **k**; n = 38,860 cells after quality control) visualized by UMAP using the list of transcription factors for feature selection. **p** Fraction of progenitor cells in each progenitor state. Values are mean ± SEM. Each data point represents an individual animal. Statistical test was performed using *propeller*. Unmarked comparisons (vs. control) did not show significant difference ($P > 0.05$).

Sup. Fig. 3

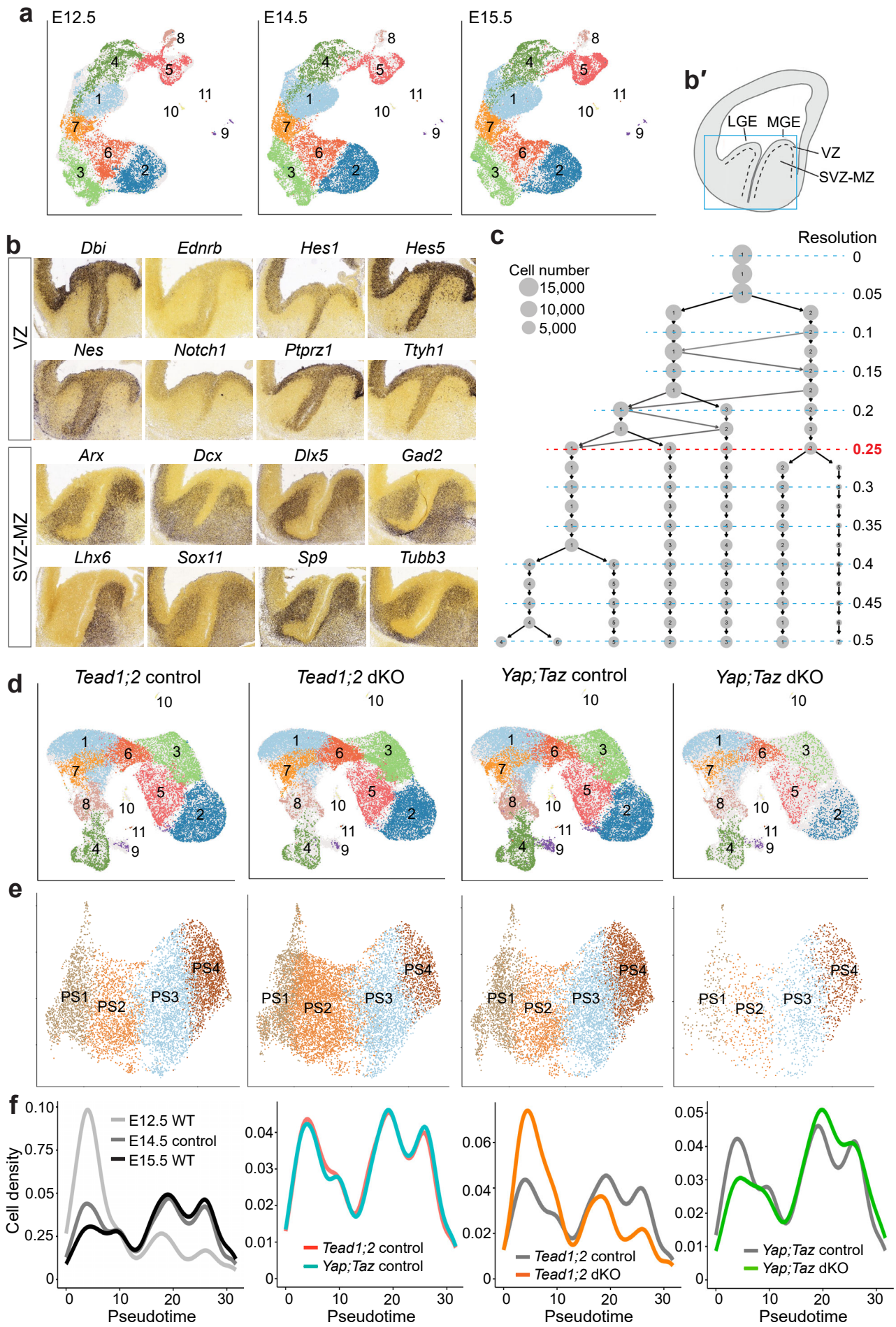
a
E12.5
E14.5
E15.5
b′
LGE
MGE
VZ
SVZ-MZ
b
Dbi
Ednrb
Hes1
Hes5
Nes
Notch1
Ptprz1
Ttyh1
Arx
Dcx
Dlx5
Gad2
Lhx6
Sox11
Sp9
Tubb3
c
Resolution
Cell number
15,000
10,000
5,000
0
0.05
0.1
0.15
0.2
0.25
0.3
0.35
0.4
0.45
0.5
d
Tead1;2 control
Tead1;2 dKO
Yap;Taz control
Yap;Taz dKO
e
PS1
PS2
PS3
PS4
f
Cell density
E12.5 WT
E14.5 control
E15.5 WT
Tead1;2 control
Yap;Taz control
Tead1;2 dKO
Yap;Taz dKO
Pseudotime

Supplementary Fig. 3 | Single-cell RNA sequencing analysis reveals distinct impacts of TEAD1/2 loss and YAP/TAZ loss on MGE neural progenitor lineage progression. a Clustering of WT MGE cells based on highly variable genes (HVG) visualized by UMAP. E12.5 WT, 11,929 cells after quality control; E14.5 *Tead1;2* control, 15,124 cells; E15.5 WT, 15,823 cells. **b** Expression patterns (from Allen Developing Mouse Brain Atlas) of selected genes in the VZ and SVZ-MZ gene lists. **b′** A schematic of the E13.5 telencephalon showing subpallial regional organization. VZ, ventricular zone; SVZ, subventricular zone; MZ, mantle zone. **c** Cluster tree analysis of WT progenitor cells showing changes in cluster composition with stepwise increase of clustering resolution. **d** Clustering of E14.5 control and dKO MGE cells based on HVG visualized by UMAP. *Tead1;2* control, 15,124 cells; *Tead1;2* dKO, 18,406 cells; *Yap;Taz* control, 18,041 cells; *Yap;Taz* dKO, 6,361 cells. **e** Progenitor state annotation of progenitor cells visualized by UMAP using the list of transcription factors for feature selection. *Tead1;2* control, 7,172 cells; *Tead1;2* dKO, 9,648 cells; *Yap;Taz* control, 8,299 cells; *Yap;Taz* dKO, 1,954 cells. **f** Pseudotime density plot of progenitor cells.

Fig. 5

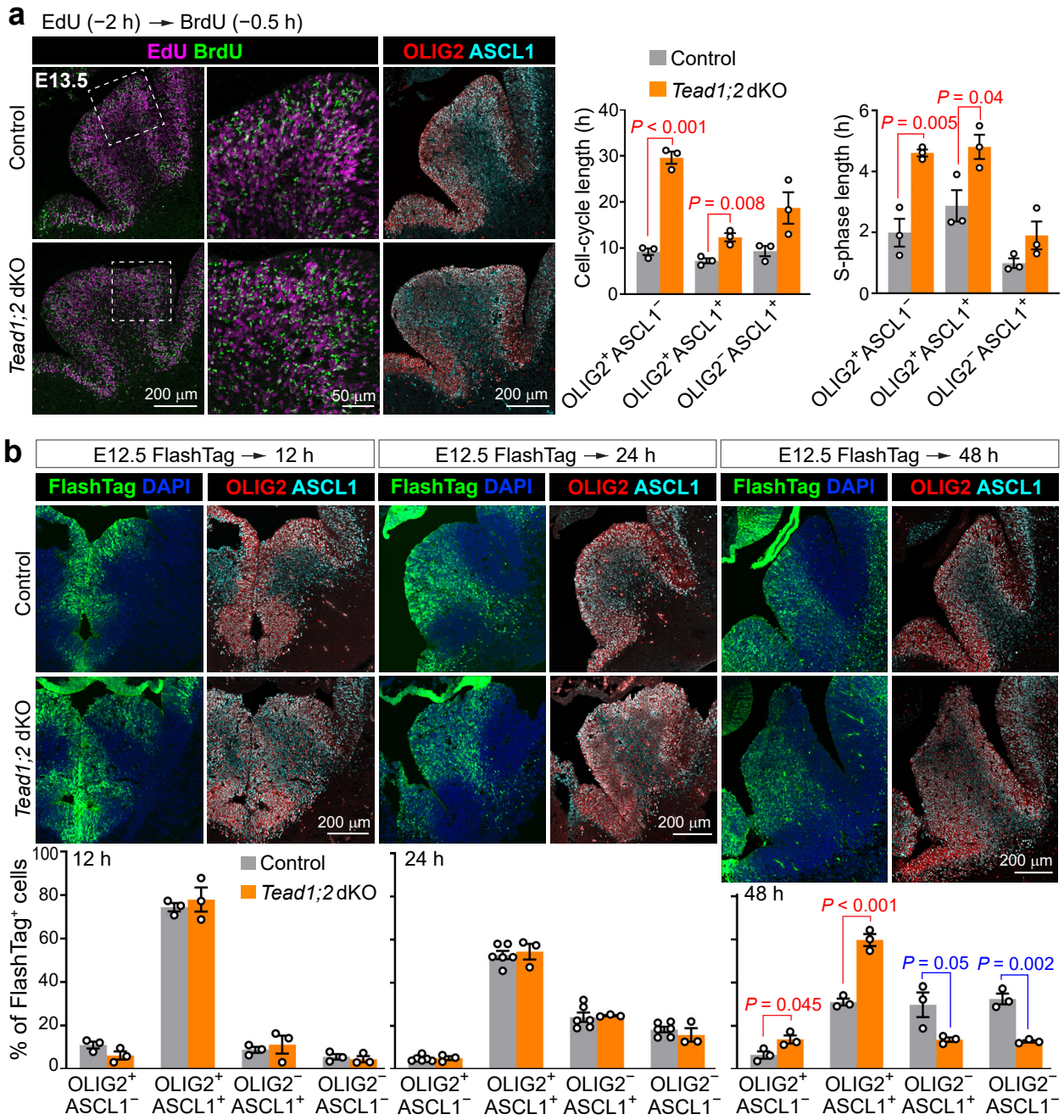

Fig. 5 | TEAD1/2 loss impedes developmental progression of subpallial neural progenitors. a Immunostaining and quantification measuring the cell cycle speed of MGE progenitor cells by EdU-BrdU sequential labeling. Areas in dashed boxes are enlarged in the images to the right. **b** Immunostaining and quantification of the fraction of FlashTag-labeled cells in each of the progenitor states defined by OLIG2 and ASCL1 immunosignal. Values are mean ± SEM. Each data point represents an individual animal. Two-sided unpaired *t*-test. Unmarked comparisons (vs. control) did not show significant difference ($P > 0.05$).

Fig. 6

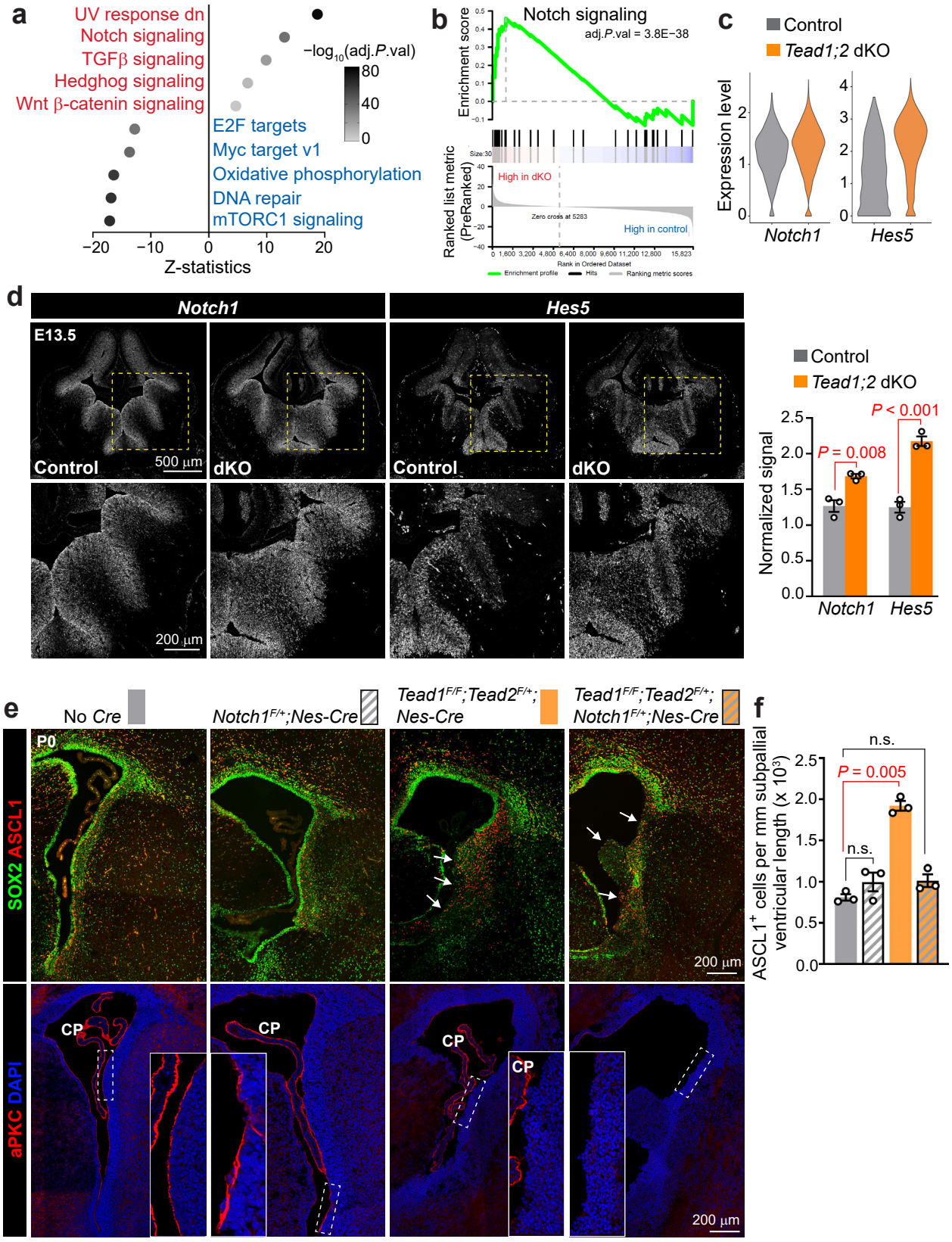
a
UV response dn
Notch signaling
TGFβ signaling
Hedghog signaling
Wnt β-catenin signaling
E2F targets
Myc target v1
Oxidative phosphorylation
DNA repair
mTORC1 signaling
−log10(adj.P.val)
80
40
0
−20
−10
0
10
20
Z-statistics
b
Notch signaling
adj.P.val = 3.8E−38
Enrichment score
Ranked list metric (PreRanked)
High in dKO
High in control
Zero cross at 5283
Rank in Ordered Dataset
Enrichment profile
Hits
Ranking metric scores
c
Control
Tead1;2 dKO
Expression level
Notch1
Hes5
d
Notch1
Hes5
E13.5
Control
dKO
Control
dKO
500 μm
200 μm
Control
Tead1;2 dKO
Normalized signal
P = 0.008
P < 0.001
Notch1
Hes5
e
No Cre
Notch1F/+;Nes-Cre
Tead1F/F;Tead2F/+;Nes-Cre
Tead1F/F;Tead2F/+;Notch1F/+;Nes-Cre
P0
SOX2 ASCL1
aPKC DAPI
CP
200 μm
f
ASCL1+ cells per mm subpallial ventricular length (x 10³)
n.s.
P = 0.005
n.s.

Fig. 6 | TEAD1/2 promote lineage progression of subpallial neural progenitors by inhibiting Notch signaling. a Top 5 enriched Hallmark gene sets by gene set enrichment analysis (GSEA) comparing *Tead1;2* dKO to control PS2 cells. **b** Enrichment plot of the Notch_signaling gene set. **c** ScRNA-seq expression levels of *Notch1* ($\log_2$FC = 0.17, adj.*P*.val = 0.001) and *Hes5* ($\log_2$FC = 2.24, adj.*P*.val = 2.8E−143) in PS2 cells comparing *Tead1;2* dKO vs. control. **d** RNAscope in situ hybridization analysis of *Notch1* and *Hes5* expression in E13.5 brain sections. Areas in dashed boxes are enlarged in the images below. Mean fluorescence intensity in the MGE (total signals divided by area) were normalized to the mean intensity in a cortical VZ region within the same section. **e** Immunostaining of neural progenitors (SOX2 and ASCL1) and apical junctions (aPKC) in P0 brain sections. Arrows highlight disruptions in the VS and VZ-SVZ organization. CP, choroid plexus. **f** Quantification of ASCL1$^+$ cells located in subpallial VZ-SVZ in P0 brain sections. Values in **d** and **f** are mean ± SEM. Two-sided unpaired *t*-test; n.s., not significant ($P > 0.05$). Each data point represents an individual animal.

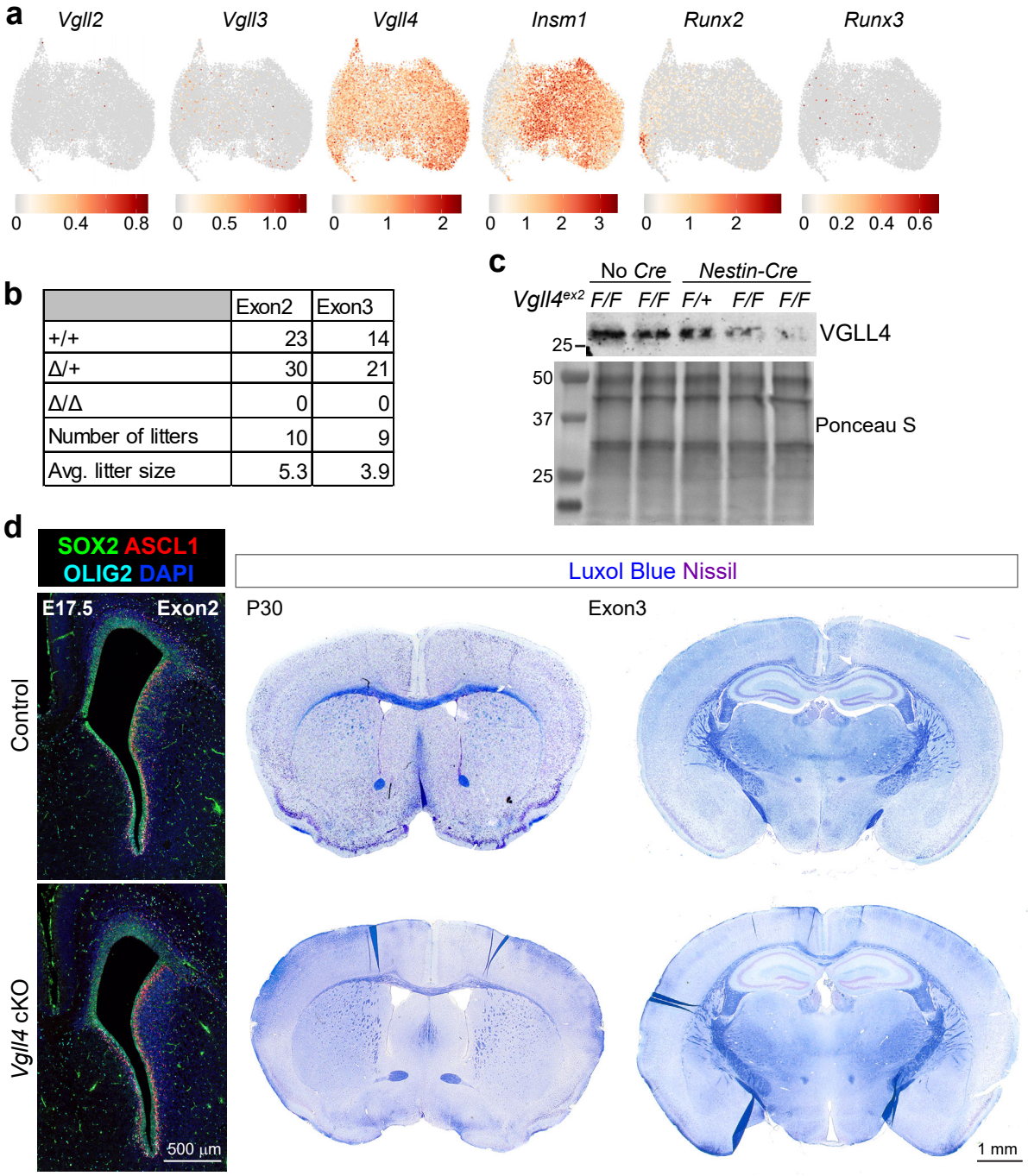

	Exon2	Exon3
+/+	23	14
Δ/+	30	21
Δ/Δ	0	0
Number of litters	10	9
Avg. litter size	5.3	3.9

Supplementary Fig. 4 | Loss of VGLL4 does not notably perturb brain development. a ScRNA-seq expression levels of genes encoding proteins known to interact with TEAD in WT progenitor cells visualized by UMAP. **b** Number of live animals genotyped from *Vgll4*$^{\Delta/+}$ x *Vgll4*$^{\Delta/+}$ breedings. Tissue biopsies were collected between P3 to P7. **c** Western blot of total brain lysates from E14.5 no-*Cre* control and *Nestin-cre*-mediated *Vgll4* conditional KO (cKO) mice deleting exon 2. **d** Gross morphology of control and *Vgll4* cKO brains. E17.5 images are obtained from exon2 cKO line. P30 images are from exon3 cKO line.

Fig. 7

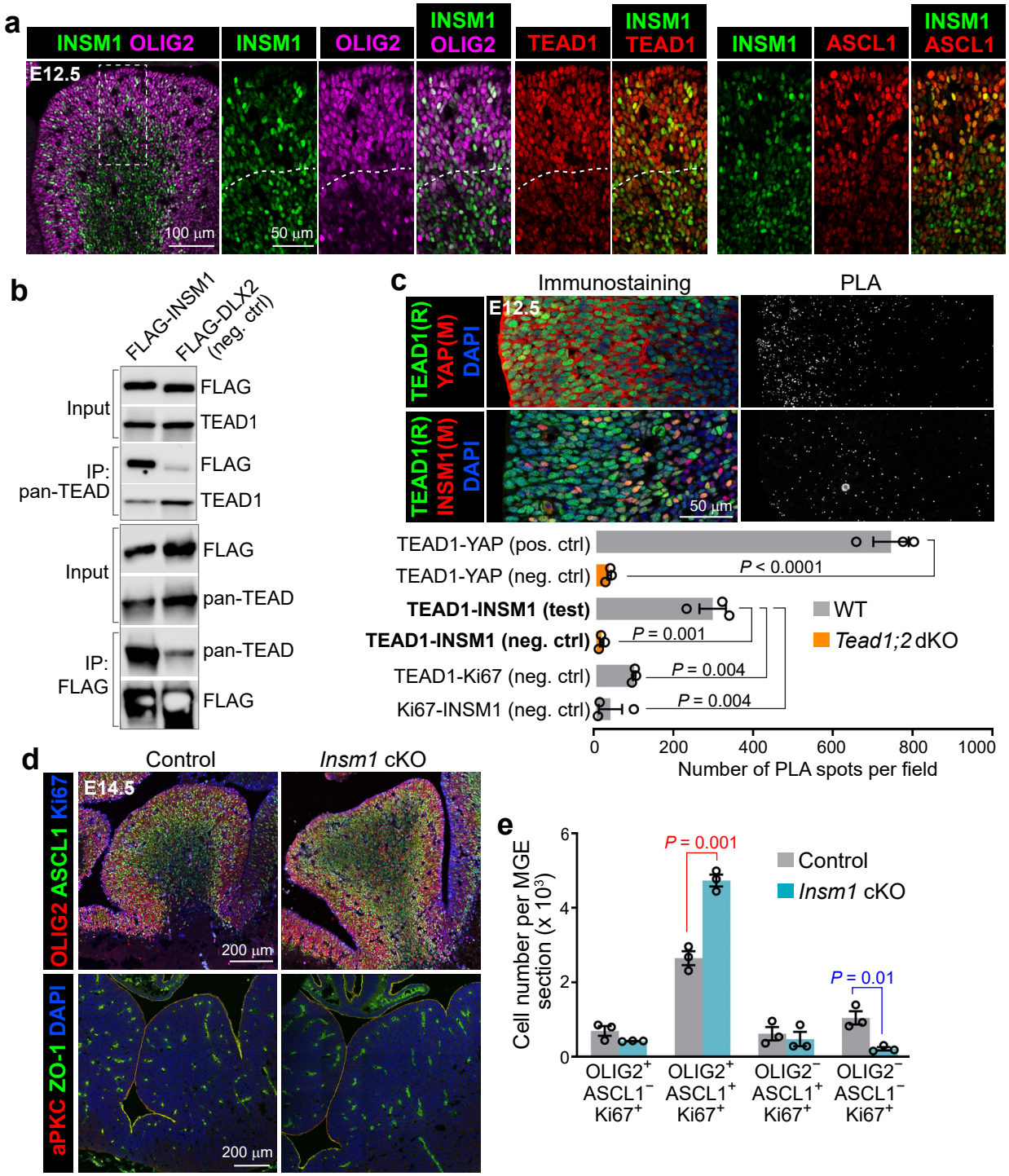

Fig. 7 | INSM1 interacts with TEAD and promote lineage progression of subpallial neural progenitors. a INSM1 expression pattern in E12.5 MGE examined by immunostaining. Dashed lines delineate VZ and SVZ boundary. **b** Co-immunoprecipitation experiment using 293T cells transfected with FLAG-tagged INSM1 or DLX2 (negative control) to examine the interaction between endogenous TEAD and FLAG-tagged proteins. **c** Examples of immunostaining and proximity ligation assay (PLA) images of adjacent E12.5 brain sections showing subpallial regions and quantification of PLA signals as fluorescent spots. (R), rabbit antibody; (M), mouse antibody. Each data point represents an individual embryo. **d** Immunostaining of neural progenitors (OLIG2 and ASCL1) and apical junctions (aPKC and ZO-1) in E14.5 MGE. **e** Quantification of progenitors in the states defined by OLIG2 and ASCL1 immunosignal. Values in c and e are mean ± SEM. Each data point represents an individual animal. Two-sided unpaired *t*-test. Unmarked comparisons (vs. control) did not show significant difference ($P > 0.05$).

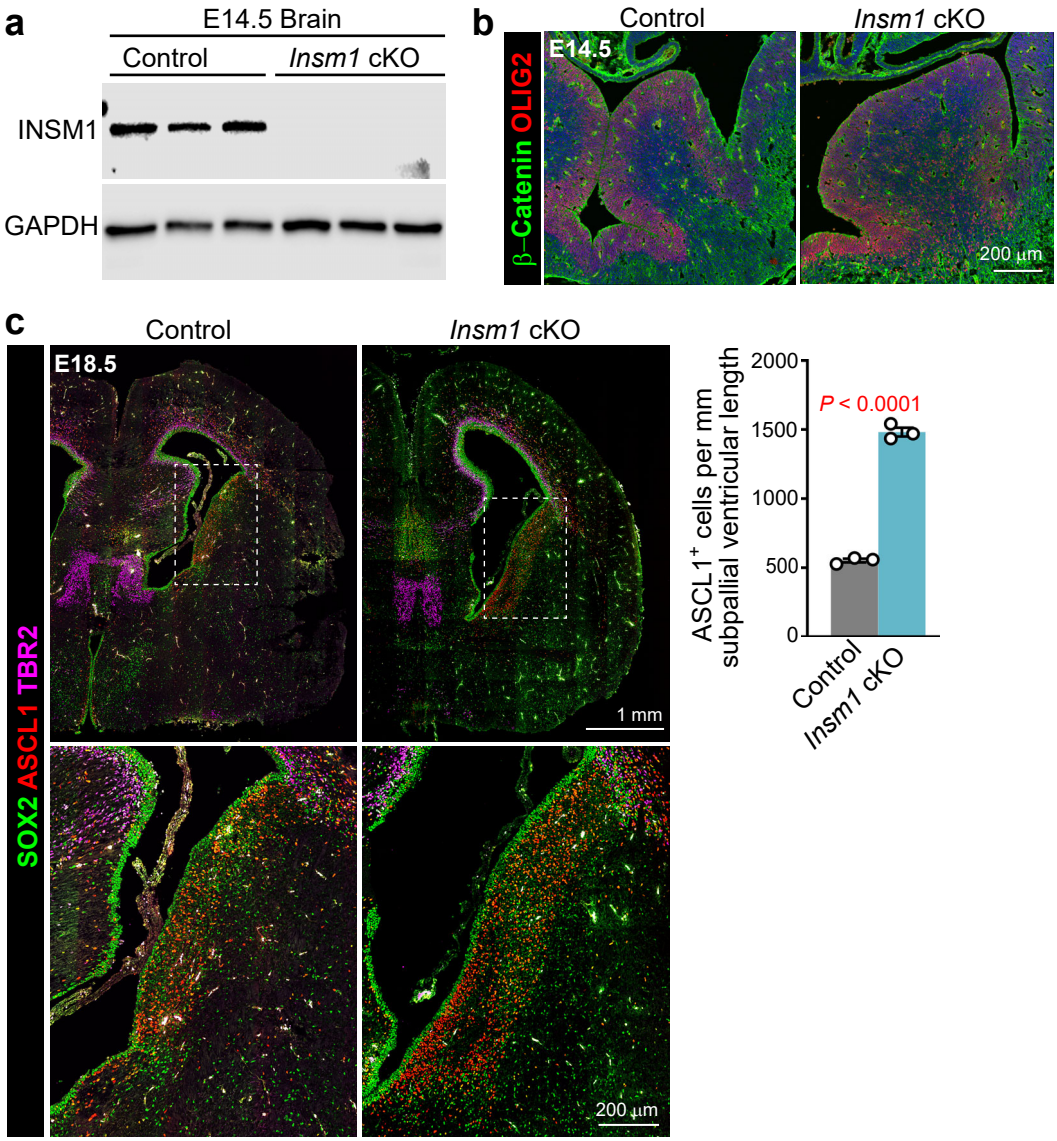

Supplementary Fig. 5 | Characterization of *Insm1* cKO mice. a Western blot of total brain lysates from no-*Cre* control and *Nestin-cre*-mediated *Insm1* conditional KO (cKO) mice. **b** Immunostaining for neural progenitor (OLIG2) and apical junction (β-catenin) markers, showing MGE regions. Blue color is DAPI signal. **c** Immunostaining of neural progenitor cells and quantification of subpallial ASCL1-labeled cells.

Fig. 8

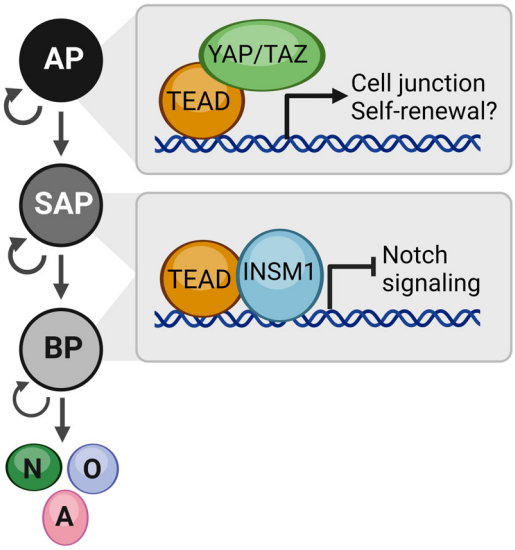

Fig. 8 | A model of TEAD function during subpallial development. During subpallial development, TEAD interacts with different partners in different progenitor subtypes/states to execute distinct functions. In apical progenitors (APs), TEAD interacts with YAP/TAZ to promote the expression of cell junction genes; whether TEAD also promotes self-renewal with YAP/TAZ remains to be determined. In subapical progenitors (SAPs) and possibly a subset of basal progenitors (BPs), TEAD interacts with INSM1 to promote lineage progression at least in part by inhibiting Notch signaling. N, neurons; O, oligodendrocytes; A, astrocytes. Created with BioRender.com.